Next Materials 9 (2025) 101277

Contents lists available at ScienceDirect

Next Materials

journal homepage: www.sciencedirect.com/journal/next-materials

Research article

Development of an App for analyzing and monitoring non-linear fluid-induced vibration of nanotube using analytical and machine learning approaches

A.A. Yinusa [a,*], J.I. Eke [a], A.R. Amokun [a], S.S. Folorunsho [b], M.G. Sobamowo [a], A. Oluwo [a], G. Oguntala [c], A.O. Adelaja [a]

[a] Department of Mechanical Engineering, University of Lagos, Akoka, Lagos, Nigeria
[b] Rensselaer Polytechnic Institute, Troy, NY, USA
[c] Department of Biomedical Engineering, Birmingham City University, UK

A R T I C L E I N F O

Keywords:
Single-walled carbon nanotube
Dynamic response
Galerkin decomposition method
Differential transform method
Cosine-after treatment
Sine-after treatment
XGBoost
Machine learning
Mobile application

A B S T R A C T

This paper investigates the dynamic response and Single-walled carbon nanotube's vibrational properties under varying conditions. This study uses a blend of theoretical modeling and empirical analysis to investigate the effects of different parameters on the behavior. The Galerkin method was used to derive and simplify the nonlinear Partial Differential Equation that represented the motion of the Single-walled carbon nanotube into an Ordinary Differential Equation. The Differential Transform Method is then used to solve the resulting Ordinary Differential Equation. The application of Cosine After-Treatment and Sine After-Treatment techniques guarantees the validity of the solution over longer time domains. The impacts of nonlocal elasticity, nonlinear foundation parameters, and mode number on the system's response are thoroughly examined. Furthermore, this study integrates machine learning to enhance the analysis and visualization of the nanotube's deflection and vibration effects. Simulated data are used to train various machine learning models using Extreme Gradient Boosting (XGBoost). The study also includes the development of a mobile application to provide an interactive platform for visualizing the nanotube's dynamic response, making the findings accessible to a broader audience. The results are relevant to nano-electromechanical systems, nanofluidic transport, nanosensors, energy harvesting devices, and medicinal systems where vibrational stability and dependability are essential. This subsequently advances the knowledge of Single-walled carbon nanotube's behavior and lay the groundwork for further studies in this field.

1. Introduction

The capacity to analyze, predict, and visualize the nonlinear dynamics of Single-walled carbon nanotubes (SWCNTs) remains a challenging and largely unexplored area, making it an attractive subject of investigation. SWCNTs are adaptable for a variety of applications due to their exceptional mechanical, thermal, and electrical properties. In biomedicine, SWCNTs are used in diagnostics, targeted therapies, and drug delivery, showing significant potential in cancer treatment and wearable health devices. SWCNTs also play a key role in energy storage, notably in fuel cells and solar energy systems, due to their vast surface area and thermal conductivity. In electronics and optoelectronics, SWCNTs are regarded as future replacements for conventional semiconductors, with applications in high-performance infrared photodetectors. They also contribute to environmental solutions, such as air and water purification, and CO2 capture. Lastly, SWCNTs are revolutionizing fabrics and fibers, enabling temperature-regulated smart fabrics that enhance thermal management and personal comfort. Flow-induced vibration in SWCNTs has a direct effect on the dependability of nanofluid transport, nano-electromechanical systems, and nanosensors, where unregulated oscillations can result in breakdown or performance loss. With practical applications in biomedical systems, environmental monitoring, and advanced materials technologies, a deeper understanding of these vibration dynamics aids in the development of stable, vibration-resistant nanodevices and energy harvesters. Lu et al. [1] investigated electronic relaxation and vibrational dynamics in SWCNTs with the use of ultrashort visible pulse laser and transient

* Corresponding author.
E-mail address: aayinusa@unilag.edu.ng (A.A. Yinusa).

https://doi.org/10.1016/j.nxmate.2025.101277
Received 23 August 2025; Received in revised form 26 September 2025; Accepted 28 September 2025
Available online 11 October 2025

Nomenclature

L	*Length*
ρ	mass density of beam
w	lateral displacement of beam
A	area of cross-section
I_0, I_1	Bessel terms
t	time
t^*	dimensionless time
P	pressure
k_1, k_2	Winkler-like elastic foundation coefficient
ρ	density of fluid
I	moment of inertia
$(e_0 a)$	non-local parameter
K	spring stiffness
B	2D Magnetic field
Ω_{CAT}	Regularisation term CATBoost
$T_b(x)$	prediction of the b-th tree for the instance x
T	the number of trees in the ensemble
w_{ij}	the weight of the j-th leaf in the i-th tree
λ_j	the L2 regularisation parameter
E	Young modulus
$U(r)$	fluid velocity distribution
m_f	mass of nanofluid
K_n	Knusden number
ϕ	downstream angle
τ	elastic stiffness matrix of classical isotropic elasticity
t_b	thickness
y_i	true label for the i-th instance
σ_{xx}	non-local stress tensor
I_s	surface moment of inertia
R_i	radius of CNT
ρ_f	fluid density
G	shear modulus
Ω_{XGB}	Regularisation term XGBoost
n_i	number of trees in the forest
$\hat{y}_i$	predicted label for the i-th instance
d	the number of leaves in each tree
Υ_L	the L1 regularization parameter
L_a	the loss function

absorption spectroscopy, focusing on intra-band and inter-band relaxation processes. Using Euler-Bernoulli theory and nonlocal elasticity, the nonlinear thermal-magneto-mechanical stability and vibration of branching nanotubes transporting nano-magnetic fluid were investigated by Yinusa and Sobamowo [2]. The derived thermos-fluidic-vibration equation was analytically solved with Galerkin decomposition and Differential Transform Method (DTM). Yinusa and Sobamowo [3] also studied the dynamic behavior of tensioned SWCNTs in thermal and pressurized environments, using Bernoulli-Euler and thermal elasticity mechanics to analyze vibration modes and deflection. The study revealed that increasing pressure enhances nanotube deflection across various vibration modes. Tugolukov and Ali [4] reviewed the enhancement of heat transfer and thermal conductivity in conventional fluids by incorporating carbon nanotubes (CNTs). Their work demonstrates how CNT concentration and temperature improve thermal properties, which could be extended to understand thermal effects in SWCNTs used in dynamic response applications. Using Euler-Bernoulli kinematics and nano-mechanics theory to simulate CNT vibrations, Mohamed and Nazira [5] examined the nonlinear stability and dynamic behaviors of CNTs in pre-buckling and post-buckling domains. The dynamics of double-walled CNTs on a Winkler–Pasternak foundation under mechanical impact, utilizing Galerkin-Bubnov method and Eringen's nonlocal elastic theory was analyzed and investigated by Herisanu et al. [6]. Miyashiro et al., [7] explored the mechanical vibration of SWCNTs with various aspect ratios, revealing that larger aspect ratios align with Bernoulli-Euler beam theory. For the purpose of simulating dynamic responses in nanotube systems, their research sheds light on the vibrational properties of SWCNTs. Oveissi et al. [8] investigated electrical energy harvesting from the vibrations of axially moving composite nanoshells carrying nanofluid. While focusing on composite structures, the study highlights the potential of harnessing vibrational energy from SWCNTs in dynamic environments. In their investigation of CNTs' medicinal uses, Ahmed et al. [9] primarily examined how they might be used to treat cancer. They also explored the diverse ways in which CNTs can be employed as carriers for therapeutic agents, and they highlighted their potential in photothermal therapy for cancer. The mechanical properties of SWCNTs using molecular dynamics simulations and Artificial Neural Networks (ANNs) were investigated by Čanađija [10]. The study focused on the influence of chirality and provided accurate predictions of mechanical properties, directly relevant to understanding SWCNT behavior under dynamic and vibrational conditions. Technically and recently, Machine Learning (ML) has demonstrated flexibility. This enables its successful implementations in problems springing out of various areas or disciplines. Consequently, Vivanco-Benavides et al. [11] explored the integration of ML in modeling the physical properties of CNTs. It emphasized the flexibility and successful application of ML across various domains, particularly in predicting material responses and describing properties of CNTs. Förster et al. [12] addressed the tedious task of identifying CNT chirality from high-resolution transmission electron microscopy (HRTEM) images. They presented a powerful Convolutional Neural Network (CNN) trained on a massive, realistic dataset of simulated images. This AI system automates chirality assignment with impressive accuracy, significantly outpacing manual methods. Innovative machine learning techniques may be helpful in gaining novel perspectives on some difficult nanomechanical challenges. Dewapriya et al. [13] explored the potential of ANNs in forecasting the fracture stress of graphene samples with defects in a range of scenarios. Lal et al. [14] also explored a critical challenge in nanoscale mechanics: predicting the "length-scale parameter" used in higher-order elasticity theories to model material behavior. Traditionally, this parameter was assumed constant for a given material, but their high-throughput molecular dynamics simulations revealed a surprising truth – it varies with factors like size, boundary conditions, and deformation level. This variability makes accurate prediction cumbersome. To address this, the researchers developed a clever three-step framework. First, they performed extensive MD simulations on diverse scenarios. Then, they used these simulations to estimate the parameter within a continuum model. Finally, they deployed ML (Gaussian process regression, support vector machines, and neural networks) to learn the complex relationships between the parameter and its influencing factors. This powerful combination eliminated the need for further expensive MD simulations for parameter prediction, opening the door to broader application of these theories in real-world nanoscale problems. Recently, Beitollahi et al. [15] investigated the effect of nanoparticle agglomeration on CNT-reinforced nanocomposites by introducing a variable length-scale parameter. Using the modified couple stress theory, the study improves prediction accuracy, validated against experimental and molecular dynamics results. The dynamic behavior of porous plates reinforced with CNTs was examined by Bousmaha et al. [16] using a p-version finite element method. Their findings highlighted how CNT distribution, porosity models, and boundary conditions alter dynamic response, guiding lightweight structural design. Gawah et al. [17] investigated the free vibration of FG-CNTRC beams on Kerr substrates using an improved first-order shear deformation theory. Results revealed that CNT distribution, volume fraction, and nonlinear dispersion patterns significantly affect vibrational characteristics, with outcomes validated against published studies. The nonlinear forced vibration response of FG-CNTRC sandwich beams with viscoelastic cores was analyzed by Youzera et al. [18], showing that CNT reinforcement patterns, boundary conditions, and core-to-skin ratios strongly influence amplitude and frequency responses. Free vibration of sandwich cylindrical shells with FG-CNTRC face sheets was studied by Youzera et al. [19] using the differential quadrature method, demonstrating that CNT distribution, thickness ratios, and end support significantly affect natural frequencies. Al-Houri et al. [20] investigated wave propagation in FG-CNTRC beams on Kerr foundations, introducing nonlinear CNT distributions via exponential models. Their results indicated that CNT volume fraction and dispersion patterns enhance stiffness and wave velocity, while foundation parameters primarily influence bending waves. A finite element approach was developed by Tounsi et al. [21] to study porous CNT-reinforced nanocomposite beams on viscoelastic foundations. The model captured the combined influence of porosity, CNT distribution, and foundation damping, showing how these factors control stiffness, damping, and dynamic responses under free and forced vibrations. Zerrouki et al. [22] investigated the buckling behavior of FG-CNTRC beams on Winkler–Pasternak foundations using a higher-order shear deformation theory. Their analysis revealed that CNT reinforcement patterns, particularly the X-beam, provided superior buckling capacity, while porosity and geometric parameters reduced overall stability. The bending and buckling behavior of porous FG-CNTRC beams supported on viscoelastic foundations was examined by Alsubaie et al. [23], who found that porosity reduces stiffness, the O-beam pattern performs weakest, and X-beam reinforcement combined with viscoelastic foundations improves resistance. Boutaleb et al. [24] investigated the buckling response of imperfect FG-CNTRC beams, accounting for porosity and CNT reinforcement distributions. Their results showed that increased porosity reduces critical buckling loads, whereas X-CNT reinforced beams offer higher resistance to instability. A porosity-dependent vibration analysis of FG-CNTRC beams was carried out by Alsubaie et al. [25], who demonstrated that porosity increases natural frequencies while damping coefficients enhance vibration performance. Their study confirmed that CNT reinforcement patterns and foundation properties significantly govern vibrational responses. Madenci et al. [26] conducted experimental tensile tests on CNT-reinforced carbon fiber composite beams, finding that 0.3 % CNT content yielded optimum tensile strength, while higher CNT concentrations reduced capacity. Comparisons with FEM results validated the experiments and showed that Halpin–Tsai predictions of Young's modulus were more accurate than the mixture rule. Also, Belabed et al. [27] developed a Quasi-3D finite element model for FG-CNTRC beams to evaluate vibration and buckling responses. The model incorporated hyperbolic warping functions without correction factors, achieving high accuracy compared to existing methods. Results demonstrated that boundary conditions, CNT distribution, and slenderness ratio substantially influence vibrational and elastic stability, highlighting the method's computational efficiency for design and optimization of nanocomposite structures.

Hussain et al. [28] analyzed the correlation between Poisson's ratio and frequency in armchair SWCNTs using Sander's shell theory and Galerkin's method, finding frequency increases with lower Poisson's ratios and nanotube indices, offering validated benchmark results. The orthotropic vibration modeling of CNTs was presented by Hussain [29], who employed nonlocal elasticity and wave propagation approaches to compute frequency variations with aspect ratios and nonlocal parameters, highlighting CNT applications in sensors, actuators, and nanoengineering systems. Ghandourah et al. [30] investigated the vibrations of double-walled CNTs using a Timoshenko-beam model combined with wave propagation, showing that frequencies depend strongly on length scale and aspect ratio while introducing a novel waviness modeling technique. The continuous element method was extended to aeroacoustic waves in confined ducts by Khadimallah et al. [31], who validated harmonic response predictions against analytical solutions, demonstrating its broader applicability to acoustics and compressible flow problems beyond traditional structural analyses. Asghar et al. [32] developed a numerical approach for zigzag DWCNTs with a nonlocal shell model, revealing that nonlocal parameters and boundary conditions significantly affect vibration characteristics, validating their approach with published literature. Hussain [33] examined the application of Kelvin's method to CNTs, deriving motion equations and frequency spectra, and demonstrated how polynomial volume fraction indices and boundary conditions influence vibrational behavior using MATLAB computations. Finally, the vibration of FG cylindrical shells with ring supports was analyzed by Hussain and Selmi [34] through the Rayleigh–Ritz method, showing that support positions and boundary conditions alter frequencies, with clamped–clamped shells exhibiting higher curves than clamped–free ones.

Karbassiyazdi et al. [35] addressed the challenge of removing poly- and perfluoroalkyl substances (PFAS) from wastewater, particularly short-chain PFAS, using artificial intelligence. Employing the XGBoost model, the research simultaneously considered material and process factors, providing accurate predictions of adsorption capacity, equilibrium, and removal. Hua et al. [36] introduced a strategy for estimating product quality in such asynchronous sampling processes, combining data-driven and knowledge-based approaches. The mobile application, created using Flutter, communicates with API created using python Flask, to provide real-time feedback and visualizations of the SWCNTs' behavior based on user inputs. The integration of the ML model into the mobile application enhances the accessibility and usability of the analysis. Through HTTP requests, the Flutter app interacts with the Flask API to process data and display predictions in an interactive and user-friendly manner. This approach ensures that complex dynamic responses and vibration patterns are effectively visualized and interpreted, facilitating a deeper understanding of SWCNTs and their behavior under various conditions. This approach aligns with current nanotechnology application techniques, utilizing cutting-edge computational tools to deliver valuable insights through an intelligent mobile platform. Sudheer Kumar et al. [37] introduced a mobile computing approach for monitoring end mill tool life by utilizing a deep-learning model. The algorithm used calculated Remaining Useful Life (RUL) and wear state from periodically taken mobile camera images. The tool wear status is recognized using a pre-trained network (GoogleNet) for feature extraction and linear regression. A mobile application displayed wear state and RUL, aiding operators in timely tool replacement decisions. The model's accuracy and robustness are demonstrated through RMSE and Correlation Coefficient (R2) metrics. Machining experiments confirm the module's capability to capture wear states and RUL for end mills. The approach offers an efficient tool wear monitoring solution for manufacturing industries without extensive investments in machine vision hardware and software. A review of earlier research reveals that no work has been published that uses analytical and machine learning techniques to comprehensively address (using an app as a visualization interface) the dynamic response and vibration characteristics of flow-induced vibration in nanotubes. Hence, the need for the present study. This study stands out for incorporating machine learning, after-treatment methods, and analytical modeling into a single framework for the analysis of SWCNT vibrations. It goes beyond theory by integrating predictive models into a mobile application that provides easily accessible, real-time visualization. This combined method improves the practical application of nonlinear nanotube dynamics in engineering systems while also advancing the understanding of their dynamics.

2. Model formulation

Consider the nanotubes (SWCNT) shown in Fig. 1.1. This tube rests on elastic foundations, and its vibration is flow-induced. The material is assumed to be embedded in a non-linear Winkler elastic foundation. Additionally, the surface effect is assumed to be negligible. In this study, the following assumptions were made:

a) The boundary conditions at both ends are simply supported.
b) The material is embedded in a non-linear Winkler elastic foundation.
c) The surface effect is assumed to be negligible.
d) The effect of non-local elasticity can be ignored along the radial direction.

To derive the equation of motion for this nanotube, we start by recalling that its *Young's modulus* is expressed as:

$$E_x = \frac{\sigma_{xx}}{\varepsilon_{xx}} \tag{1}$$

Then the *stress* is given as:

$$\sigma_x = E\varepsilon_{xx} \tag{2}$$

The *nonlocal elasticity* theory is given as;

$$\left(1-(e_0a)^2\nabla^2\right)\sigma = \tau \tag{3}$$

Which, on simplifying, gives;

$$\sigma_{xx} - (e_0a)^2\frac{\partial^2 w}{\partial x^2} = E\varepsilon_{xx} \tag{4}$$

Recall that the *bending moment (M)* is given as:

$$M = \int_A Z\sigma_{xx}dA$$

With Z is the lateral coordinate

The *axial strain* ε_{xx} for minimal deflections is expressed as:

$$EI\frac{\partial^4 w}{\partial x^4} - (e_0a)^2\left(\begin{array}{l}\left(\left(m_n+m_f\right)\dfrac{\partial^4 w}{\partial x^2\partial t^2}\right) + \left(PA+T+m_f\nu^2-\eta H_x^2A\right)\dfrac{\partial^4 w}{\partial x^4} \\ +2m_f\nu\dfrac{\partial^4 w}{\partial x^3\partial t} + \left(k_1+3w^2k_2\right)\dfrac{\partial^2 w}{\partial x^2} + 6wk_2\left[\dfrac{\partial w}{\partial x}\right]^2\end{array}\right)$$
$$+\left(\left(m_n+m_f\right)\frac{\partial^2 w}{\partial t^2} + \left(PA+T+m_f\nu^2-\eta H_x^2A\right)\frac{\partial^2 w}{\partial x^2} + 2m_f\nu\frac{\partial^2 w}{\partial x\partial t} + k_1w + k_2w^3\right) = 0 \tag{13}$$

$$\varepsilon_{xx} = -\frac{Z\partial^2 w}{\partial x^2}$$

The *Moment of Inertia* I is given as:

$$I = \int_A Z^2 dA$$

The *force* Q is given as:

$$Q = -\frac{\partial M}{\partial x}$$

Therefore, the total of all forces acting on the nanotube is the differential

$$\frac{\partial Q}{\partial x} = -\frac{\partial^2 M}{\partial x^2} \tag{5}$$

Multiply each term in Eq. 4 by ZdA

$$Z\sigma_{xx}dA - (e_0a)^2\frac{\partial^2 Z\sigma_{xx}dA}{\partial x^2} = E\varepsilon_{xx}ZdA \tag{6}$$

Integrating $\int_A$ each term in Eq. 6 gives:

$$\int_A Z\sigma_{xx}dA - (e_0a)^2\frac{\partial^2}{\partial x^2}\int_A Z\sigma_{xx}dA = E\int_A Z\left(-\frac{Z\partial^2 w}{\partial x^2}\right)dA \tag{7}$$

Rearranging Eq. 7 gives:

$$\int_A Z\sigma_{xx}dA - (e_0a)^2\frac{\partial^2}{\partial x^2}\int_A Z\sigma_{xx}dA = -E\frac{\partial^2 w}{\partial x^2}\int_A Z^2dA \tag{8}$$

Substitute Eqs. 5a, 5b, and 5c, into Eq. 8

$$M - (e_0a)^2\frac{\partial^2 M}{\partial x^2} = -EI\frac{\partial^2 w}{\partial x^2} \tag{9}$$

Differentiating Eq. 9 twice gives:

$$\frac{d^2M}{dx^2} - (e_0a)^2\frac{\partial^2}{\partial x^2}\left(\frac{d^2M}{dx^2}\right) = -EI\frac{\partial^4 w}{\partial x^4} \tag{10}$$

This is further simplified into a generalized equation as:

$$\left(-\frac{dQ}{dx}\right) - (e_0a)^2\frac{\partial^2}{\partial x^2}\left(-\frac{dQ}{dx}\right) = -EI\frac{\partial^4 w}{\partial x^4} \tag{11}$$

The *total force* acting on the Single-Walled Carbon Nanotube is given as:

$$\frac{dQ}{dx} = \left(m_n+m_f\right)\frac{\partial^2 w}{\partial t^2} + \left(PA+T+m_f\nu^2-\eta H_x^2A\right)\frac{\partial^2 w}{\partial x^2} + 2m_f\nu\frac{\partial^2 w}{\partial x\partial t} + k_1w + k_2w^3 \tag{12}$$

By substituting the total forces acting on the single-wall carbon nanotube, considering the forces acting on the nanotube, forces due to the fluid flow, forces due to tension and magnetic effects, and forces due to the foundation, the equation is given as:

Therefore, Eq. (13) gives the governing equation for the vibration of the SWCNT.

3. The developed models and their analytical solutions

The resultant vibration model, in Eq. (13), contains nonlinear components that make it challenging to achieve a closed-form solution. In this work, the PDE is transformed into an ODE using the Galerkin Decomposition Method, and the nonlinear equation is solved analytically through DTM.

3.1. Converting the pde into ode using Galerkin's method

The Galerkin method is a numerical method used for approximating solutions to differential equations, particularly PDEs. It belongs to the class of weighted residual methods, which involve minimizing the residual of the governing equation over a certain space of functions.

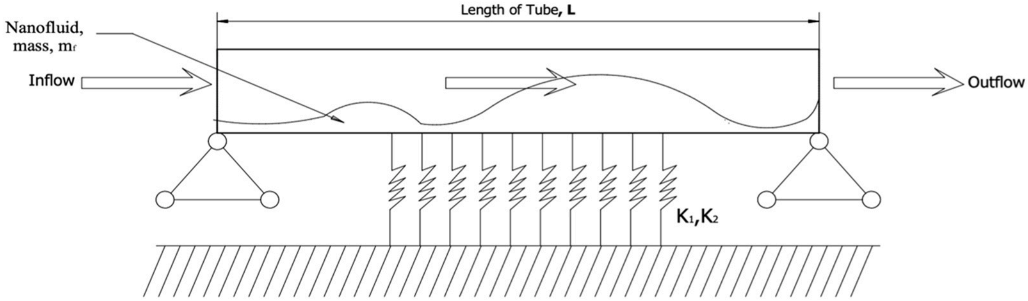

Fig. 1.1. Problem schematic of a SWCNT resting on an elastic foundation.

The Galerkin's approach is thus utilized in transforming the partial differential equation (PDE) (13) to an ODE.

Hence, the system's vibrational response can be expressed in terms of the first Eigen function $\Phi(x)$ including the generalized coordinate $q(t)$ as follows:

$$w(x,t) = \Phi(x)\cdot q(t) \tag{14}$$

Substitute Eq. 13 into Eq. 14:

$$\left[\begin{array}{l} EI\dfrac{\partial^4(\Phi(x)\cdot q(t))}{\partial x^4} - (e_0 a)^2 \left[\begin{array}{l} (m_n+m_f)\dfrac{\partial^4(\Phi(x)\cdot q(t))}{\partial x^2 \partial t^2} \\ +(PA-T+m_f\nu^2-\eta H_x^2 A)\dfrac{\partial^4(\Phi(x)\cdot q(t))}{\partial x^4} \\ +2m_f\nu\dfrac{\partial^4(\Phi(x)\cdot q(t))}{\partial x^3 \partial t} \\ +(k_1+3(\Phi(x)\cdot q(t))^2 k_2)\dfrac{\partial^2(\Phi(x)\cdot q(t))}{\partial x^2} \\ +6(\Phi(x)\cdot q(t))k_2\left[\dfrac{\partial(\Phi(x)\cdot q(t))}{\partial x}\right]^2 \end{array}\right] \\ + \left[\begin{array}{l} (m_n+m_f)\dfrac{\partial^2(\Phi(x)\cdot q(t))}{\partial t^2} + (PA-T+m_f\nu^2-\eta H_x^2 A)\dfrac{\partial^2(\Phi(x)\cdot q(t))}{\partial x^2} \\ +2m_f\nu\dfrac{\partial^2(\Phi(x)\cdot q(t))}{\partial x \partial t} \\ +k_1(\Phi(x)\cdot q(t)) + k_2(\Phi(x)\cdot q(t))^3 \end{array}\right] \end{array}\right] \\ = 0 \tag{15}$$

By resolving and re-arranging Eq. (15), we get Eq. (16) below:

$$\left[\begin{array}{l} \left[(m_n+m_f) - (e_0 a)^2\left((m_n+m_f)\dfrac{\partial^2\Phi(x)}{\partial x^2}\right)\right]\ddot{q}(t) \\ +\left[2m_f\nu\dfrac{\partial\Phi(x)}{\partial x} - (e_0 a)^2\left(2m_f\nu\dfrac{\partial^3\Phi(x)}{\partial x^3}\right)\right]\dot{q}(t) \\ +\left[\begin{array}{l} EI\dfrac{\partial^4\Phi(x)}{\partial x^4} - (e_0 a)^2\left(\left(\begin{array}{l} PA-T+m_f\nu^2 \\ -\eta H_x^2 A \end{array}\right)\dfrac{\partial^4\Phi(x)}{\partial x^4} + k_1\dfrac{\partial^2\Phi(x)}{\partial x^2}\right) \\ +(PA-T+m_f\nu^2-\eta H_x^2 A)\dfrac{\partial^2\Phi(x)}{\partial x^2} + k_1\Phi(x) \end{array}\right] q(t) \\ +\left[k_2\Phi^3(x) - (e_0 a)^2\left(3\Phi^2(x)k_2\dfrac{\partial^2\Phi(x)}{\partial x^2} + 6\Phi(x)k_2\left[\dfrac{\partial\Phi(x)}{\partial x}\right]^2\right)\right]q^3(t) \end{array}\right] \\ = 0 \tag{16}$$

Let $R_i(x,t)$ be equal to the governing Eq. (16)

Multiply each term in the governing equation by $\Phi(x)$ And integrate the resulting equation over the interval (0, L). This gives the equation below:

$$\int_0^L \left[\begin{array}{l} \left[(m_n+m_f) - (e_0 a)^2\left((m_n+m_f)\dfrac{\partial^2\Phi(x)}{\partial x^2}\right)\right]\ddot{q}(t) \\ +\left[2m_f\nu\dfrac{\partial\Phi(x)}{\partial x} - (e_0 a)^2\left(2m_f\nu\dfrac{\partial^3\Phi(x)}{\partial x^3}\right)\right]\dot{q}(t) \\ +\left[\begin{array}{l} EI\dfrac{\partial^4\Phi(x)}{\partial x^4} - (e_0 a)^2\left(\begin{array}{l} \left(\begin{array}{l} PA-T+m_f\nu^2 \\ -\eta H_x^2 A \end{array}\right)\dfrac{\partial^4\Phi(x)}{\partial x^4} \\ +k_1\dfrac{\partial^2\Phi(x)}{\partial x^2} \end{array}\right) \\ +(PA-T+m_f\nu^2-\eta H_x^2 A)\dfrac{\partial^2\Phi(x)}{\partial x^2} + k_1\Phi(x) \end{array}\right] q(t) \\ +\left[-(e_0 a)^2\left(3\Phi^2(x)k_2\dfrac{\partial^2\Phi(x)}{\partial x^2} + 6\Phi(x)k_2\left[\dfrac{\partial\Phi(x)}{\partial x}\right]^2\right) + k_2\Phi^3(x)\right]q^3(t) \end{array}\right]\Phi(x)dx = 0 \tag{17}$$

Therefore, we now perform a term-by-term conversion of the above equation to turn it into an ODE.

1st Term:

$$\int_0^L \begin{bmatrix} -(e_0a)^2\left(\left(m_n+m_f\right)\dfrac{\partial^2\Phi(x)}{\partial x^2}\right) \\ +\left(m_n+m_f\right) \end{bmatrix}\ddot{q}(t)\Phi(x)dx = \left[\int_0^L \begin{bmatrix} -(e_0a)^2\Phi(x)\left(\left(m_n+m_f\right)\dfrac{\partial^2\Phi(x)}{\partial x^2}\right) \\ +\left(m_n+m_f\right)\Phi(x) \end{bmatrix}dx\right]\ddot{q}(t) \tag{18}$$

2nd Term:

$$\int_0^L \left[-(e_0a)^2\left(2m_f\nu\frac{\partial^3\Phi(x)}{\partial x^3}\right)+2m_f\nu\frac{\partial\Phi(x)}{\partial x}\right]\dot{q}(t)\Phi(x)dx = \left[\int_0^L \begin{bmatrix} -(e_0a)^2\Phi(x)\left(2m_f\nu\dfrac{\partial^3\Phi(x)}{\partial x^3}\right) \\ +2m_f\nu\Phi(x)\dfrac{\partial\Phi(x)}{\partial x} \end{bmatrix}dx\right]\dot{q}(t) \tag{19}$$

3rd Term:

$$\int_0^L \begin{bmatrix} EI\dfrac{\partial^4\Phi(x)}{\partial x^4}-(e_0a)^2\begin{pmatrix} \left(PA-T+m_f\nu^2-\eta H_x^2A\right)\dfrac{\partial^4\Phi(x)}{\partial x^4} \\ +k_1\dfrac{\partial^2\Phi(x)}{\partial x^2} \end{pmatrix} \\ +\left(PA-T+m_f\nu^2-\eta H_x^2A\right)\dfrac{\partial^2\Phi(x)}{\partial x^2}+k_1\Phi(x) \end{bmatrix}q(t)\Phi(x)dx = \left[\int_0^L \begin{bmatrix} EI\Phi(x)\dfrac{\partial^4\Phi(x)}{\partial x^4}-(e_0a)^2\Phi(x)\begin{pmatrix} \left(PA-T+m_f\nu^2-\eta H_x^2A\right)\dfrac{\partial^4\Phi(x)}{\partial x^4} \\ +k_1\dfrac{\partial^2\Phi(x)}{\partial x^2} \end{pmatrix} \\ +\left(PA-T+m_f\nu^2-\eta H_x^2A\right)\Phi(x)\dfrac{\partial^2\Phi(x)}{\partial x^2}+k_1\Phi^2(x) \end{bmatrix}dx\right]q(x) \tag{20}$$

4th Term:

$$\int_0^L \begin{bmatrix} -(e_0a)^2\left(3\Phi^2(x)k_2\dfrac{\partial^2\Phi(x)}{\partial x^2}+6\Phi(x)k_2\left[\dfrac{\partial\Phi(x)}{\partial x}\right]^2\right) \\ +k_2\Phi^3(x) \end{bmatrix}q^3(t)\Phi(x)dx = \left[\int_0^L \begin{bmatrix} -(e_0a)^2\left(3\Phi^3(x)k_2\dfrac{\partial^2\Phi(x)}{\partial x^2}+6\Phi^2(x)k_2\left[\dfrac{\partial\Phi(x)}{\partial x}\right]^2\right) \\ +k_2\Phi^4(x) \end{bmatrix}dx\right]q^3(t) \tag{21}$$

Rearranging and grouping like terms, the Galerkin method produces the Duffing equation below:

$$M\ddot{q}(t)+C\dot{q}(t)+K_1q(t)+K_2q^3(t)=0 \tag{22}$$

Where M, C, K_1, and K_2 are constant parameters and given as:

Table 4.1
Table of CAT technique iterations at mode 1.

θ_1	θ_2	λ_1	λ_2
−3.8835e+ 15	−5.9225e+ 15	3.5000e−10	−4.5168e−27
3.8835e+ 15	−5.9225e+ 15	3.5000e−10	−4.5168e−27
−3.8835e+ 15	5.9225e+ 15	3.5000e−10	−4.5168e−27
3.8835e+ 15	5.9225e+ 15	3.5000e−10	−4.5168e−27
−5.9225e+ 15	−3.8835e+ 15	−4.5168e−27	3.5000e−10
5.9225e+ 15	−3.8835e+ 15	−4.5168e−27	3.5000e−10
−5.9225e+ 15	3.8835e+ 15	−4.5168e−27	3.5000e−10
5.9225e+ 15	3.8835e+ 15	−4.5168e−27	3.5000e−10

$$M=\left[\begin{array}{l}\int_0^L\left[-(e_0a)^2\Phi(x)\left((m_n+m_f)\frac{\partial^2\Phi(x)}{\partial x^2}\right)+(m_n+m_f)\Phi(x)\right]dx\\ =\int_0^L\Phi(x)\left[-(e_0a)^2\left((m_n+m_f)\frac{\partial^2\Phi(x)}{\partial x^2}\right)+(m_n+m_f)\right]dx\end{array}\right] \tag{23}$$

The value of C is given as:

$$C=\left[\begin{array}{l}\int_0^L\left[-(e_0a)^2\Phi(x)\left(2m_f\nu\frac{\partial^3\Phi(x)}{\partial x^3}\right)+2m_f\nu\Phi(x)\frac{\partial\Phi(x)}{\partial x}\right]dx\\ =\int_0^L\Phi(x)\left[-(e_0a)^2\left(2m_f\nu\frac{\partial^3\Phi(x)}{\partial x^3}\right)+2m_f\nu\frac{\partial\Phi(x)}{\partial x}\right]dx\end{array}\right] \tag{24}$$

Also, the value of K_1 is given as:

$$K_1=\left[\begin{array}{l}\int_0^L\left[\begin{array}{l}EI\Phi(x)\frac{\partial^4\Phi(x)}{\partial x^4}-(e_0a)^2\Phi(x)\left(\begin{array}{l}(PA-T+m_f\nu^2-\eta H_x^2A)\frac{\partial^4\Phi(x)}{\partial x^4}\\ +k_1\frac{\partial^2\Phi(x)}{\partial x^2}\end{array}\right)\\ +(PA-T+m_f\nu^2-\eta H_x^2A)\Phi(x)\frac{\partial^2\Phi(x)}{\partial x^2}+k_1\Phi^2(x)\end{array}\right]dx\\ =\int_0^L\Phi(x)\left(\begin{array}{l}EI\frac{\partial^4\Phi(x)}{\partial x^4}-(e_0a)^2\left(\begin{array}{l}(PA-T+m_f\nu^2-\eta H_x^2A)\frac{\partial^4\Phi(x)}{\partial x^4}\\ +k_1\frac{\partial^2\Phi(x)}{\partial x^2}\end{array}\right)\\ +(PA-T+m_f\nu^2-\eta H_x^2A)\frac{\partial^2\Phi(x)}{\partial x^2}+k_1\Phi(x)\end{array}\right)dx\end{array}\right] \tag{25}$$

The value of constant K_2 is given as:

$$K_2=\left[\begin{array}{l}\int_0^L\left[\begin{array}{l}-(e_0a)^2\left(3\Phi^3(x)k_2\frac{\partial^2\Phi(x)}{\partial x^2}+6\Phi^2(x)k_2\left[\frac{\partial\Phi(x)}{\partial x}\right]^2\right)\\ +k_2\Phi^4(x)\end{array}\right]dx\\ =\int_0^L\Phi(x)\left(\begin{array}{l}-(e_0a)^2\left(3\Phi^2(x)k_2\frac{\partial^2\Phi(x)}{\partial x^2}+6\Phi(x)k_2\left(\frac{\partial\Phi(x)}{\partial x}\right)^2\right)\\ +k_2\Phi^3(x)\end{array}\right)dx\end{array}\right] \tag{26}$$

Determining the model's natural frequency, it is obtained as:

$$\omega_n=\sqrt{\frac{K_1}{M}} \tag{27}$$

Substituting Eqs. (23) and (25) into Eq. (27) gives:

$$\omega_n=\sqrt{\frac{\int_0^L\Phi(x)\left(\begin{array}{l}EI\frac{\partial^4\Phi(x)}{\partial x^4}-(e_0a)^2\left(\begin{array}{l}(PA-T+m_f\nu^2-\eta H_x^2A)\frac{\partial^4\Phi(x)}{\partial x^4}\\ +k_1\frac{\partial^2\Phi(x)}{\partial x^2}\end{array}\right)\\ +(PA-T+m_f\nu^2-\eta H_x^2A)\frac{\partial^2\Phi(x)}{\partial x^2}+k_1\Phi(x)\end{array}\right)dx}{\int_0^L\Phi(x)\left[-(e_0a)^2\left((m_n+m_f)\frac{\partial^2\Phi(x)}{\partial x^2}\right)+(m_n+m_f)\right]dx}} \tag{28}$$

Where, ω_n is the Model's Natural frequency.

Eq. (22) is the expected system of ODE from Galerkin's decomposition of the PDEs, which is afterwards solved using DTM.

3.2. Model solution using differential transform method

By applying the principle of DTM as illustrated in some previous works [2,3] to the Duffing model expressed as Eq. (22), we obtain:

$$\left[\begin{array}{l}M[(k+1)(k+2)q[k+2]]+C[(k+1)q[k+1]]+K_1[q[k]]\\ -K_2\left[\sum_{p=0}^{k}\sum_{l=0}^{p}q[l]q[p-l]q[k-p]\right]\end{array}\right]=0 \tag{29}$$

This can be rewritten as:

$$M[(k+1)(k+2)q[k+2]]=\left(\begin{array}{l}K_2\left[\sum_{p=0}^{k}\sum_{l=0}^{p}q[l]q[p-l]q[k-p]\right]\\ -C[(k+1)q[k+1]]-K_1[q[k]]\end{array}\right) \tag{30}$$

Making the highest coefficient of q the subject of the formula from Eq. (30):

$$\therefore q[k+2]=\frac{\left[K_2\left[\sum_{p=0}^{k}\sum_{l=0}^{p}q[l]q[p-l]q[k-p]\right]-C[(k+1)q[k+1]]-K_1[q[k]]\right]}{M(k+1)(k+2)} \tag{31}$$

Given the initial conditions to be:

Let the initial displacement q be$q=\beta$, $q[0]=\beta$

Then the initial velocity $\dot{q}$will be$\dot{q}=0$, $\dot{q}=q[1]=0$

Iterating the governing Eq. (31) for $k=0$, 1, 2, 3, and 4 gives the following value for$q[k]$:

At $k=1$, we have:

$$q_2=\frac{K_2\beta^3-K_1\beta}{2M} \tag{32}$$

At $k=2$:

$$q_3=-\frac{1}{6M}\left[\frac{C(K_2\beta^3-K_1\beta)}{M}\right] \tag{33}$$

At $k=3$:

$$q_4 = \frac{1}{12M}\left[\frac{3K_2\beta^2\left(K_2\beta^3 - K_1\beta\right)}{2M} - \frac{K_1\left(K_2\beta^3 - K_1\beta\right)}{2M} + \frac{C^2\left(K_2\beta^3 - K_1\beta\right)}{2M^2}\right] \tag{34}$$

At $k = 4$:

$$q_5 = \frac{1}{20M}\left[-\frac{K_2\beta^2 C\left(K_2\beta^3 - K_1\beta\right)}{2M^2} + \frac{K_1 C\left(K_2\beta^3 - K_1\beta\right)}{6M^2} - \frac{C\left(\frac{3K_2\beta^2\left(K_2\beta^3 - K_1\beta\right)}{2M} - \frac{K_1\left(K_2\beta^3 - K_1\beta\right)}{2M} + \frac{C^2\left(K_2\beta^3 - K_1\beta\right)}{2M^2}\right)}{3M}\right] \tag{35}$$

At $k = 5$:

$$q_6 = \frac{1}{30M}\left[K_2\left(\frac{\beta^2\left(\frac{3K_2\beta^2\left(K_2\beta^3 - K_1\beta\right)}{2M} - \frac{K_1\left(K_2\beta^3 - K_1\beta\right)}{2M} + \frac{C^2\left(K_2\beta^3 - K_1\beta\right)}{2M^2}\right)}{4M} + \frac{3\beta\left(K_2\beta^3 - K_1\beta\right)^2}{4M^2}\right) - \frac{K_1\left(\frac{3K_2\beta^2\left(K_2\beta^3 - K_1\beta\right)}{2M} - \frac{K_1\left(K_2\beta^3 - K_1\beta\right)}{2M} + \frac{C^2\left(K_2\beta^3 - K_1\beta\right)}{2M^2}\right)}{12M} - \frac{C\left(-\frac{K_2\beta^2 C\left(K_2\beta^3 - K_1\beta\right)}{2M^2} + \frac{K_1 C\left(K_2\beta^3 - K_1\beta\right)}{6M^2} - \frac{C\left(\frac{3K_2\beta^2\left(K_2\beta^3 - K_1\beta\right)}{2M} - \frac{K_1\left(K_2\beta^3 - K_1\beta\right)}{2M} + \frac{C^2\left(K_2\beta^3 - K_1\beta\right)}{2M^2}\right)}{3M}\right)}{4M}\right] \tag{36}$$

Table 4.4
Table of SAT technique iterations at mode 1.

ψ_1	ψ_2	μ_1	μ_2
−5.2433e+ 15	5.2433e+ 15	−1.0950e−51	1.0950e−51
5.2433e+ 15	5.2433e+ 15	1.0950e−51	1.0950e−51
−5.2433e+ 15	5.2433e+ 15	−1.0950e−51	1.0950e−51
5.2433e+ 15	5.2433e+ 15	1.0950e−51	1.0950e−51
−5.2433e+ 15	−5.2433e+ 15	−1.0950e−51	−1.0950e−51
5.2433e+ 15	−5.2433e+ 15	1.0950e−51	−1.0950e−51
−5.2433e+ 15	−5.2433e+ 15	−1.0950e−51	−1.0950e−51
5.2433e+ 15	−5.2433e+ 15	1.0950e−51	−1.0950e−51

Table 4.2
Table of CAT technique iterations at mode 2.

θ_1	θ_2	λ_1	λ_2
−5.1273e+ 16	−0.0000e+ 00	3.5000e−10	−6.3230e−27
5.1273e+ 16	−0.0000e+ 00	3.5000e−10	−6.3230e−27
−5.1273e+ 16	0.0000e+ 00	3.5000e−10	−6.3230e−27
5.1273e+ 16	0.0000e+ 00	3.5000e−10	−6.3230e−27
−0.0000e+ 00	−5.1273e+ 16	−6.3230e−27	3.5000e−10
0.0000e+ 00	−5.1273e+ 16	−6.3230e−27	3.5000e−10
−0.0000e+ 00	5.1273e+ 16	−6.3230e−27	3.5000e−10
0.0000e+ 00	5.1273e+ 16	−6.3230e−27	3.5000e−10

Table 4.3
Table of CAT technique iterations at mode 3.

θ_1	θ_2	λ_1	λ_2
−7.1082e+ 15	−7.1549e+ 15	3.5000e−10	2.1377e−22
7.1082e+ 15	−7.1549e+ 15	3.5000e−10	2.1377e−22
−7.1082e+ 15	7.1549e+ 15	3.5000e−10	2.1377e−22
7.1082e+ 15	7.1549e+ 15	3.5000e−10	2.1377e−22
−7.1549e+ 15	−7.1082e+ 15	2.1377e−22	3.5000e−10
7.1549e+ 15	−7.1082e+ 15	2.1377e−22	3.5000e−10
−7.1549e+ 15	7.1082e+ 15	2.1377e−22	3.5000e−10
7.1549e+ 15	7.1082e+ 15	2.1377e−22	3.5000e−10

At $k = 6$

$$q_7 = -\frac{1}{42M}\Bigg[K_2\left(-\frac{1}{20M}\left(3\beta^2\left(-\frac{K_2\beta^2C(K_2\beta^3-K_1\beta)}{2M^2}+\frac{K_1C(K_2\beta^3-K_1\beta)}{6M^2}-\frac{C\left(\frac{3K_2\beta^2(K_2\beta^3-K_1\beta)}{2M}-\frac{K_1(K_2\beta^3-K_1\beta)}{2M}+\frac{C^2(K_2\beta^3-K_1\beta)}{2M^2}\right)}{3M}\right)\right)-\frac{\beta C(K_2\beta^3-K_1\beta)^2}{2M^3}\right)$$
$$-\frac{1}{20M}\left(K_1\left(-\frac{K_2\beta^2C(K_2\beta^3-K_1\beta)}{2M^2}+\frac{K_1C(K_2\beta^3-K_1\beta)}{6M^2}-\frac{C\left(\frac{3K_2\beta^2(K_2\beta^3-K_1\beta)}{2M}-\frac{K_1(K_2\beta^3-K_1\beta)}{2M}+\frac{C^2(K_2\beta^3-K_1\beta)}{2M^2}\right)}{3M}\right)\right)$$
$$K_2\left(\frac{\beta^2\left(\frac{3K_2\beta^2(K_2\beta^3-K_1\beta)}{2M}-\frac{K_1(K_2\beta^3-K_1\beta)}{2M}+\frac{C^2(K_2\beta^3-K_1\beta)}{2M^2}\right)}{4M}+\frac{3\beta(K_2\beta^3+K_1\beta)^2}{4M^2}\right)$$
$$-\frac{1}{5M}\left(C\left(-\frac{K_1\left(\frac{3K_2\beta^2(K_2\beta^3-K_1\beta)}{2M}-\frac{K_1(K_2\beta^3-K_1\beta)}{2M}+\frac{C^2(K_2\beta^3-K_1\beta)}{2M^2}\right)}{12M}-\frac{1}{4M}\left(C\left(-\frac{K_2\beta^2C(K_2\beta^3-K_1\beta)}{2M^2}+\frac{K_1C(K_2\beta^3-K_1\beta)}{6M^2}-\frac{C\left(\frac{3K_2\beta^2(K_2\beta^3-K_1\beta)}{2M}-\frac{K_1(K_2\beta^3-K_1\beta)}{2M}+\frac{C^2(K_2\beta^3-K_1\beta)}{2M^2}\right)}{3M}\right)\right)\right)\right)\Bigg] \tag{37}$$

The expression for the lateral displacement of the CNT as a function of the time passed is given as:

$$q[t] = \sum_{i=0}^{k} q_i t^i = q_0 + q_1 t + q_2 t^2 + q_3 t^3 + q_4 t^4 + \ldots + q_k t^k \tag{38}$$

For k = 5, we have:

$$q[t] = \sum_{i=0}^{5} q_i t^i = q_0 + q_1 t + q_2 t^2 + q_3 t^3 + q_4 t^4 + q_5 t^5 \tag{39}$$

Therefore, we have,

$$q[t] = \left[\begin{array}{l} \beta - \frac{(K_2\beta^3-K_1\beta)t^2}{2M} - \frac{C(K_2\beta^3-K_1\beta)t^3}{6M^2} \\ + \frac{\left(\frac{3K_2\beta^2(K_2\beta^3-K_1\beta)}{2M}-\frac{K_1(K_2\beta^3-K_1\beta)}{2M}+\frac{C^2(K_2\beta^3-K_1\beta)}{2M^2}\right)t^4}{12M} \\ + \frac{\left(-\frac{K_2\beta^2C(K_2\beta^3-K_1\beta)}{2M^2}+\frac{K_1C(K_2\beta^3-K_1\beta)}{6M^2}-\frac{C\left(\frac{3K_2\beta^2(K_2\beta^3-K_1\beta)}{2M}-\frac{K_1(K_2\beta^3-K_1\beta)}{2M}+\frac{C^2(K_2\beta^3-K_1\beta)}{2M^2}\right)}{3M}\right)t^5}{20M} \end{array}\right] \tag{40}$$

Eq. (40) is the DTM solution of the Duffing equation q[t].

The displacement equation $w(x,t)$ is then calculated as:

Recall that:

$$w(x,t) = \Phi(x)\cdot q(t) \tag{41}$$

Substituting the value of $q(t)$ in Eq. (41) gives:

$$w\left(x,t\right) = \left[\beta - \frac{\left(K_2\beta^3 - K_1\beta\right)t^2}{2M} - \frac{C\left(K_2\beta^3 - K_1\beta\right)t^3}{6M^2} + \frac{\left(\frac{3K_2\beta^2\left(K_2\beta^3 - K_1\beta\right)}{2M} - \frac{K_1\left(K_2\beta^3 - K_1\beta\right)}{2M} + \frac{C^2\left(K_2\beta^3 - K_1\beta\right)}{2M^2}\right)t^4}{12M} + \frac{\left(-\frac{K_2\beta^2C\left(K_2\beta^3 - K_1\beta\right)}{2M^2} + \frac{K_1C\left(K_2\beta^3 - K_1\beta\right)}{6M^2} - \frac{C\left(\frac{3K_2\beta^2\left(K_2\beta^3 - K_1\beta\right)}{2M} - \frac{K_1\left(K_2\beta^3 - K_1\beta\right)}{2M} + \frac{C^2\left(K_2\beta^3 - K_1\beta\right)}{2M^2}\right)}{3M}\right)t^5}{20M}\right]\Phi(x) \tag{42}$$

In this project, the CNT is subjected to a simply supported end condition. This means that:

$$\Phi(x) = \sin\left(\frac{n\pi}{L}x\right) \tag{43}$$

Where, $\Phi(x)$is the Phase angle or the mode shape function.

Substituting Eq. (43) into Eq. (42) we have,

$$w\left(x,t\right) = \left[\beta - \frac{\left(K_2\beta^3 - K_1\beta\right)t^2}{2M} - \frac{C\left(K_2\beta^3 - K_1\beta\right)t^3}{6M^2} + \frac{\left(\frac{3K_2\beta^2\left(K_2\beta^3 - K_1\beta\right)}{2M} - \frac{K_1\left(K_2\beta^3 - K_1\beta\right)}{2M} + \frac{C^2\left(K_2\beta^3 - K_1\beta\right)}{2M^2}\right)t^4}{12M} + \frac{\left(-\frac{K_2\beta^2C\left(K_2\beta^3 - K_1\beta\right)}{2M^2} + \frac{K_1C\left(K_2\beta^3 - K_1\beta\right)}{6M^2} - \frac{C\left(\frac{3K_2\beta^2\left(K_2\beta^3 - K_1\beta\right)}{2M} - \frac{K_1\left(K_2\beta^3 - K_1\beta\right)}{2M} + \frac{C^2\left(K_2\beta^3 - K_1\beta\right)}{2M^2}\right)}{3M}\right)t^5}{20M}\right]\sin\left(\frac{n\pi}{L}x\right) \tag{44}$$

Therefore, the constants M, C, K_1, and K_2 are obtained as:

$$M = -\frac{\left(\left(\frac{\pi^2\ \sin(\pi n)a^2n^2}{2} + L^2\right)\cos(\pi n) - \frac{\pi^3a^2n^3}{2} - L^2\right)\left(m_n + m_f\right)}{\pi nL} \tag{45}$$

$$C = \frac{\sin\ (\pi n)^2 v m_f\left(\pi^2a^2n^2 + L^2\right)}{L^2} \tag{46}$$

$$K_1 = \frac{\left(-\cos(n\pi)\sin(n\pi) + n\pi\right)\left(\begin{array}{l} n^4\left(\left(\left(H^2\eta - P\right)A - m_f v^2 + T\right)e_0a^2 + EI\right)\pi^4 \\ +\left(e_0a^2k_1 + \left(H^2\eta - P\right)A - m_f v^2 + T\right)L^2n^2\pi^2 \\ +k_1L^4 \end{array}\right)}{2L^3n\pi} \tag{47}$$

Table 4.5
Table of SAT technique iterations at mode 2.

ψ_1	ψ_2	μ_1	μ_2
−6.9226e+ 16	6.9226e+ 16	−5.6218e−50	5.6218e−50
6.9226e+ 16	6.9226e+ 16	5.6218e−50	5.6218e−50
−6.9226e+ 16	6.9226e+ 16	−5.6218e−50	5.6218e−50
6.9226e+ 16	6.9226e+ 16	5.6218e−50	5.6218e−50
−6.9226e+ 16	−6.9226e+ 16	−5.6218e−50	−5.6218e−50
6.9226e+ 16	−6.9226e+ 16	5.6218e−50	−5.6218e−50
−6.9226e+ 16	−6.9226e+ 16	−5.6218e−50	−5.6218e−50
6.9226e+ 16	−6.9226e+ 16	5.6218e−50	−5.6218e−50

Table 4.6
Table of SAT technique iterations at mode 3.

ψ_1	ψ_2	μ_1	μ_2
−9.5971e+ 15	−9.5971e+ 15	−1.5788e−50	−1.5788e−50
9.5971e+ 15	−9.5971e+ 15	1.5788e−50	−1.5788e−50
−9.5971e+ 15	−9.5971e+ 15	−1.5788e−50	−1.5788e−50
9.5971e+ 15	−9.5971e+ 15	1.5788e−50	−1.5788e−50
−9.5971e+ 15	9.5971e+ 15	−1.5788e−50	1.5788e−50
9.5971e+ 15	9.5971e+ 15	1.5788e−50	1.5788e−50
−9.5971e+ 15	9.5971e+ 15	−1.5788e−50	1.5788e−50

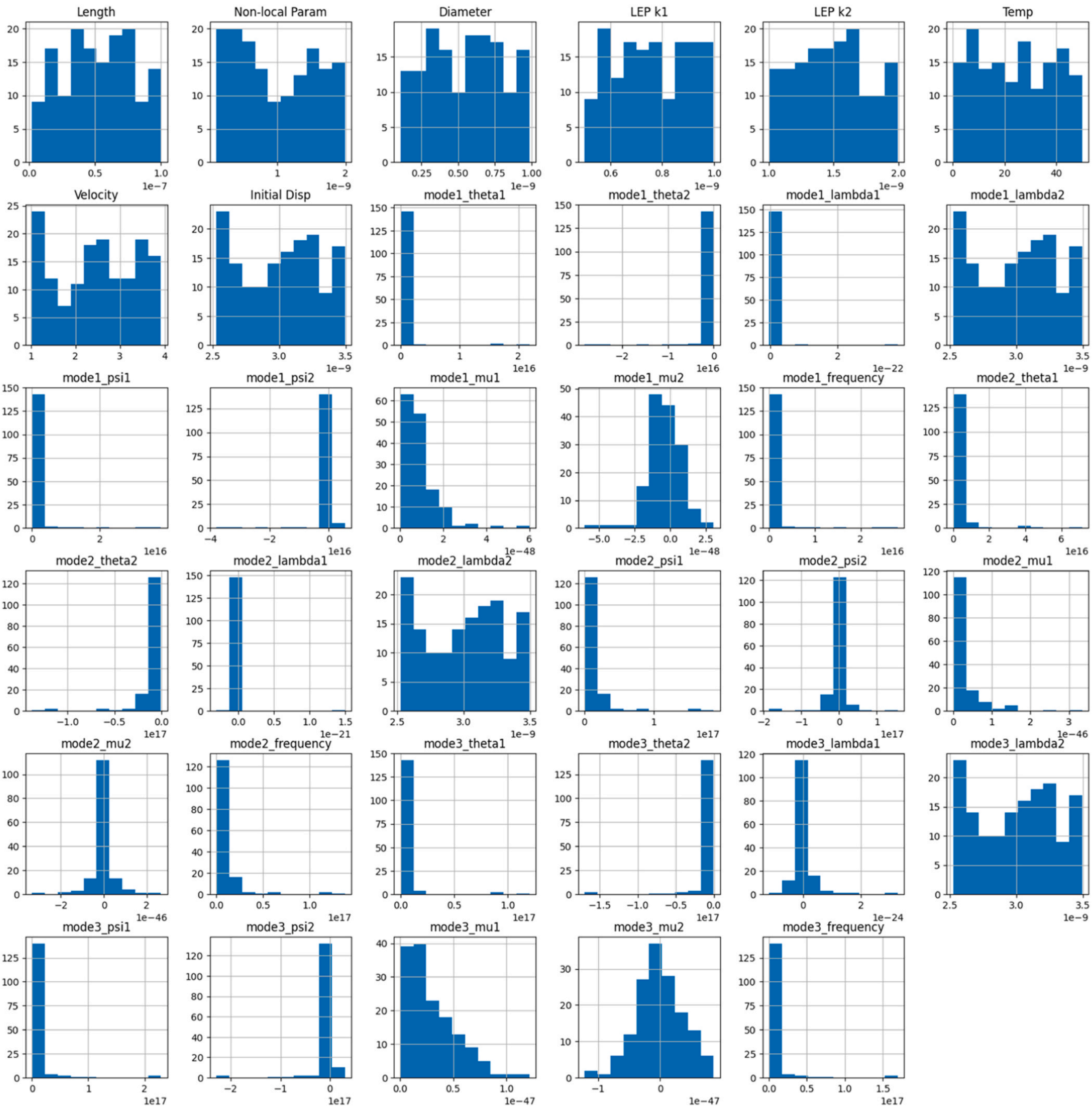

Fig. 3.1. Statistical exploration of modes.

$$K_2 = \frac{\begin{pmatrix} 2\left(6(e_0a)^2n^2\left(k_2+\frac{1}{2}\right)\pi^2+k_2L^2\right)\sin(n\pi)\cos\,(n\pi)^3 \\ -5\left(\frac{6(e_0a)^2\left(k_2+\frac{5}{2}\right)n^2\pi^2}{5}+k_2L^2\right)\sin(n\pi)\cos(n\pi) \\ +3\pi n\left(-2(e_0a)^2\left(k_2-\frac{3}{2}\right)n^2\pi^2+k_2L^2\right)\end{pmatrix}}{8Ln\pi} \tag{48}$$

Then the natural frequency is solved and is obtained as:

$$\omega_n = \sqrt{\frac{\frac{(-\cos(n\pi)\sin(n\pi)+n\pi)\begin{pmatrix} n^4\left(\left(\left(H^2\eta-P\right)A-m_fv^2+T\right)e_0a^2+EI\right)\pi^4 \\ +\left(e_0a^2k_1+\left(H^2\eta-P\right)A-m_fv^2+T\right)L^2n^2\pi^2 \\ +k_1L^4\end{pmatrix}}{2L^3n\pi}}{-\frac{\left(m_n+m_f\right)\left(\left(\frac{\sin(n\pi)(e_0a)^2n^2\pi^2}{2}+L^2\right)\cos(n\pi)-\frac{(e_0a)^2n^3\pi^3}{2}-L^2\right)}{Ln\pi}}} \tag{49}$$

3.3. *Development of after treatment techniques*

To overcome this limitation with approximate analytical solutions, an after-treatment technique (AT) must be utilized to create approximate periodic solutions over a large range of solutions. The flow-induced

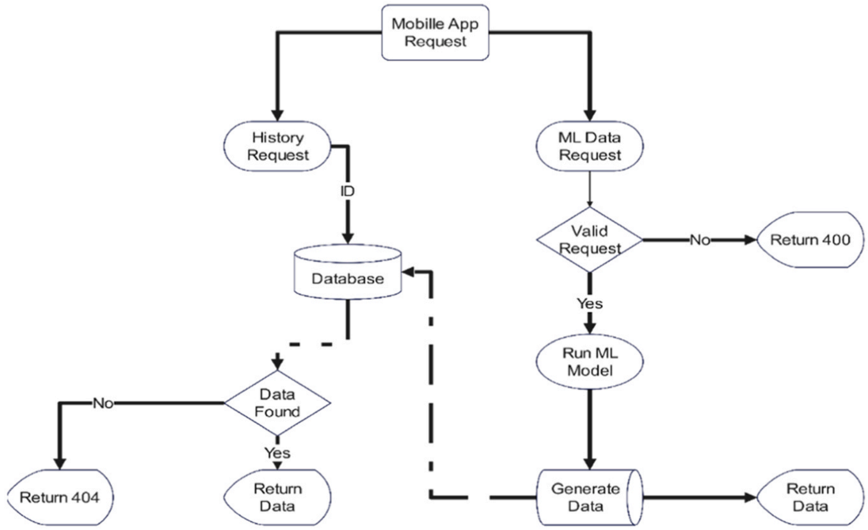

Fig. 3.2. Backend development flow-chart with Python Flask.

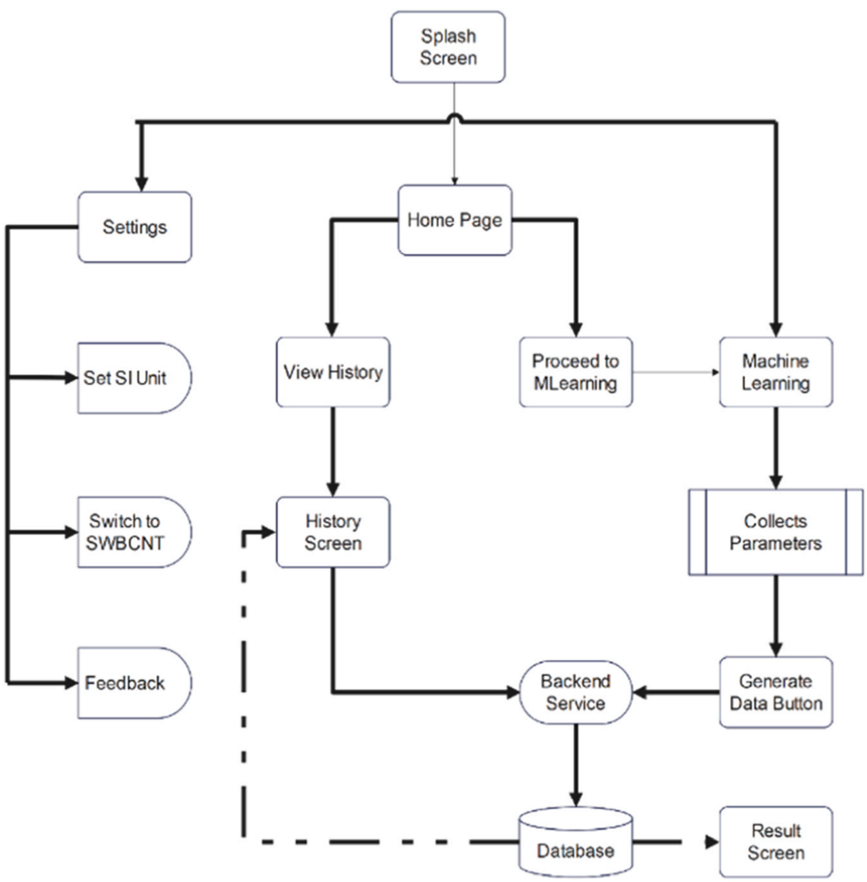

Fig. 3.3. Mobile development flow chart with Flutter.

damped vibration in this study exhibits a truncated series that is periodic only in a narrow domain. In this study, the CAT and SAT after-treatment procedures are utilized to make the solution periodic over a wide range.

3.3.1. *Cosine-after treatment technique (CAT)*

This is used for a DTM transformation of a dynamic equation with an even power. Examine the following series that has been truncated in N terms:

$$\varphi_N(t) = \sum_{k=0}^{N} q_k t^k$$

Where $\varphi_N(t)$ is the DTM's truncated series solution.

Considering that the equation can be expressed in even power terms as follows:

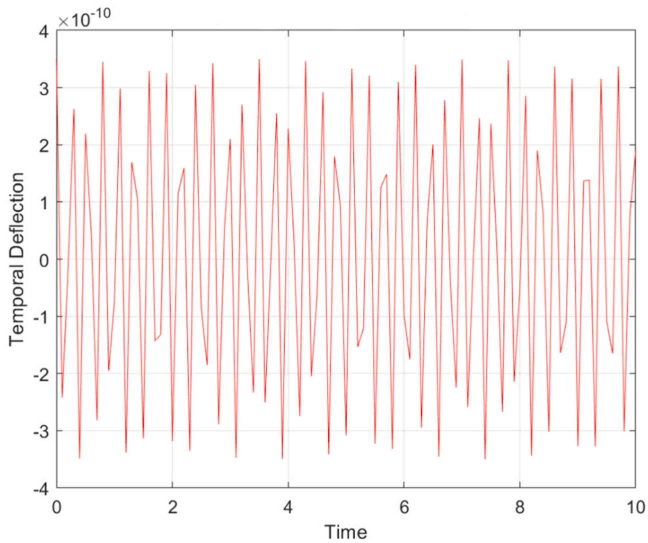

Fig. 4.1. SWCNT's Dynamic Response at Mode 1.

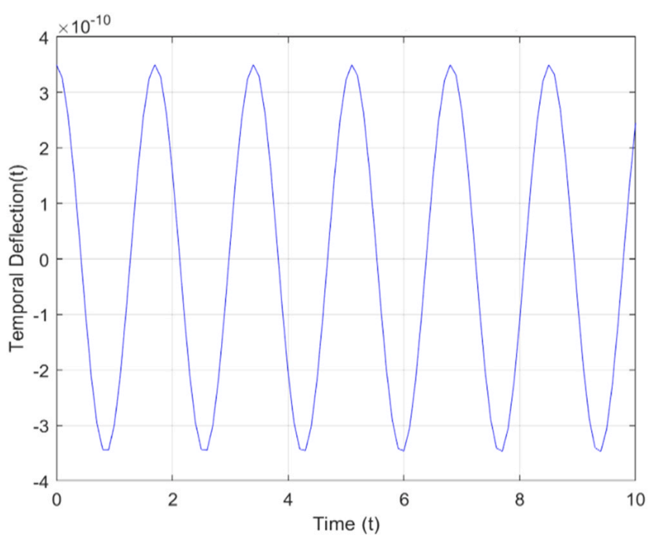

Fig. 4.2. SWCNT's Dynamic Response at Mode 2.

$$\varphi_N(t) = \sum_{k=0}^{N} q_{2k} t^{2k}$$

This is put through:

$$\forall k = 0, 1, 2, \cdots, \frac{N}{2} - 1$$

The Cosine equivalent equation is therefore provided as:

$$\varphi_N(t) = \sum_{k=0}^{n} \lambda_k \cos(\theta_k t) \tag{50}$$

Then, using Fourier series expansion, it becomes:

$$\varphi_N(t) = \sum_{k=1}^{n} \lambda_k - \left(\sum_{k=1}^{n} \lambda_k \theta_k^2\right) \frac{t^2}{2!} + \left(\sum_{k=1}^{n} \lambda_k \theta_k^4\right) \frac{t^4}{4!} - \left(\sum_{k=1}^{n} \lambda_k \theta_k^6\right) \frac{t^6}{6!} + \left(\sum_{k=1}^{n} \lambda_k \theta_k^8\right) \frac{t^8}{8!} - \cdots \tag{51}$$

The series solution of Eq. (50b) is given as:

$$\varphi_N(t) = q_0 + q_2 t^2 + q_4 t^4 + q_6 t^6 + \cdots + q_N t^N \tag{52}$$

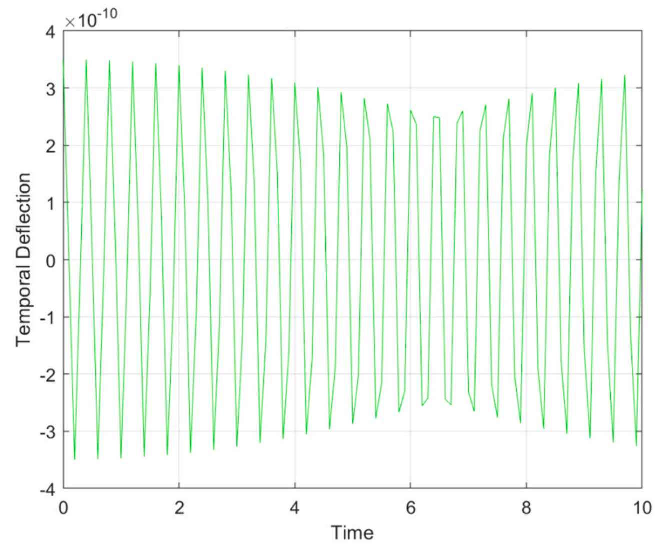

Fig. 4.3. SWCNT's Dynamic Response at Mode 3.

By comparing both series solutions, we have:

$$q_0 + q_2 t^2 + q_4 t^4 + q_6 t^6 + \cdots + q_N t^N = \sum_{k=1}^{n} \lambda_k - \left(\sum_{k=1}^{n} \lambda_k \theta_k^2\right) \frac{t^2}{2!} + \left(\sum_{k=1}^{n} \lambda_k \theta_k^4\right) \frac{t^4}{4!} - \left(\sum_{k=1}^{n} \lambda_k \theta_k^6\right) \frac{t^6}{6!} + \cdots \tag{53}$$

By comparing coefficients, we have:

$$\begin{aligned} t^0 &: \sum_{k=1}^{n} \lambda_k = q_0 \\ t^2 &: \sum_{k=1}^{n} \lambda_k \theta^2 = -2! q_2 \\ t^4 &: \sum_{k=1}^{n} \lambda_k \theta^4 = 4! q_4 \\ t^6 &: \sum_{k=1}^{n} \lambda_k \theta^6 = -6! q_6 \end{aligned} \tag{54}$$

An approximation of the expression in the form of a Cos function is given in place of these terms. This technique is described for the instance in which the truncation order (N) is 6. The goal is to express a function with two terms of Cosine functions (n = 2). Which is:

$$\varphi_N(t) = \sum_{k=1}^{2} \lambda_k \cos(\theta_k t) = \lambda_1 \cos(\theta_1 t) + \lambda_2 \cos(\theta_2 t) \tag{55}$$

Applying the technique/approach to Eq. (54) gives:

$$\begin{aligned} t^0 &: \lambda_1 + \lambda_2 = q_0 \\ t^2 &: \lambda_1 {\theta_1}^2 + \lambda_2 {\theta_2}^2 = -2! q_2 \\ t^4 &: \lambda_1 {\theta_1}^4 + \lambda_2 {\theta_2}^4 = 4! q_4 \\ t^6 &: \lambda_1 {\theta_1}^6 + \lambda_2 {\theta_2}^6 = -6! q_6 \end{aligned} \tag{56}$$

The four unknowns$\lambda_1, \lambda_2, \theta_1, \theta_2$ were obtained by providing solutions to the above system of nonlinear algebraic equations numerically.

From Eq. (32 - 37), the values of q were calculated thus:

Substituting the q values into the CAT equation, we have:

Mode n = 1

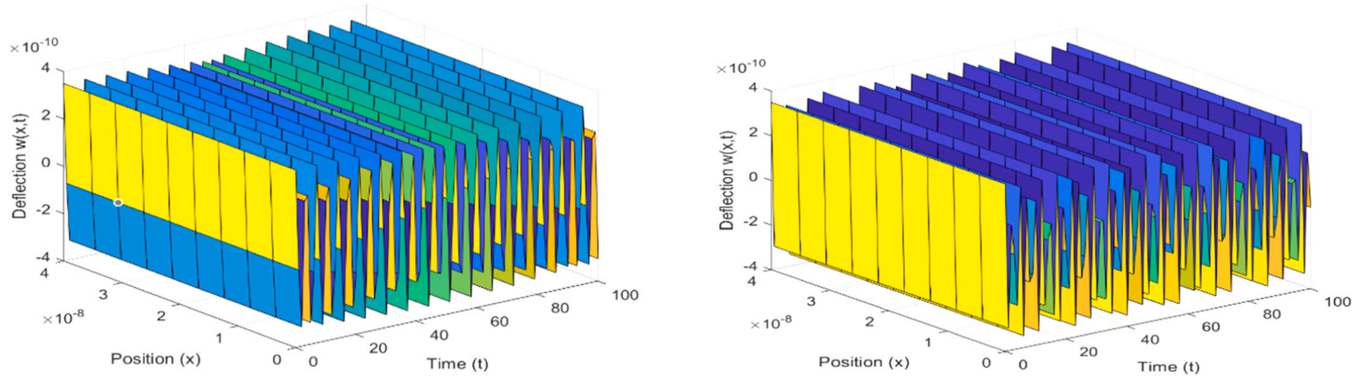

Fig 4.4. 3-D SWCNT's dynamic response at Mode 1.

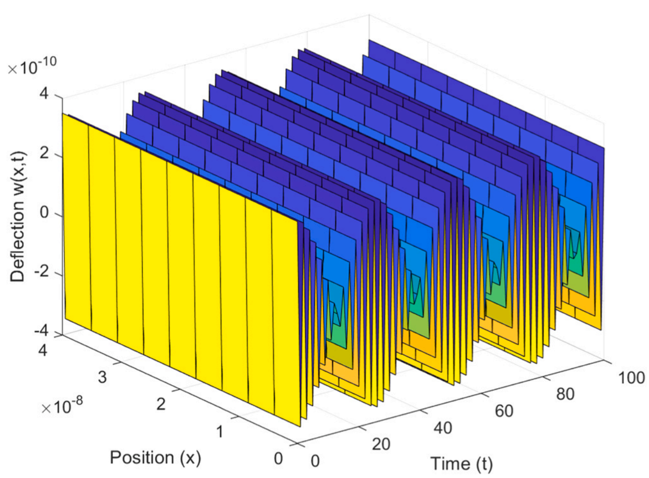

Fig 4.5. 3-D SWCNT's dynamic response at Mode 2.

$$\begin{aligned}
&\lambda_1 + \lambda_2 = 3.5000 \times 10^{-10}\\
&\lambda_1{\theta_1}^2 + \lambda_2{\theta_2}^2 = -2.6393 \times 10^{21}\\
&\lambda_1{\theta_1}^4 + \lambda_2{\theta_2}^4 = 3.3171 \times 10^{51}\\
&\lambda_1{\theta_1}^6 + \lambda_2{\theta_2}^6 = -1.6676 \times 10^{81}
\end{aligned} \tag{57-1}$$

Mode n = 2

$$\begin{aligned}
&\lambda_1 + \lambda_2 = 3.5000 \times 10^{-10}\\
&\lambda_1{\theta_1}^2 + \lambda_2{\theta_2}^2 = -4.6006 \times 10^{23}\\
&\lambda_1{\theta_1}^4 + \lambda_2{\theta_2}^4 = 1.0079 \times 10^{56}\\
&\lambda_1{\theta_1}^6 + \lambda_2{\theta_2}^6 = -8.8322 \times 10^{87}
\end{aligned} \tag{57-2}$$

Mode n = 3

$$\begin{aligned}
&\lambda_1 + \lambda_2 = 3.5000 \times 10^{-10}\\
&\lambda_1{\theta_1}^2 + \lambda_2{\theta_2}^2 = -8.8422 \times 10^{21}\\
&\lambda_1{\theta_1}^4 + \lambda_2{\theta_2}^4 = 3.7231 \times 10^{52}\\
&\lambda_1{\theta_1}^6 + \lambda_2{\theta_2}^6 = -6.2706 \times 10^{82}
\end{aligned} \tag{57-3}$$

Eqs. (57–1 – 57–3) are further solved simultaneously to yield the results in Table 4.1-4.6

3.3.2. *Sine-after treatment technique (SAT technique)*

When odd-power terms appear in the DTM series solutions, the SAT technique is applied. Examine the following series that has been truncated in N terms:

$$\varphi_N(t) = \sum_{k=0}^{N} q_k t^k \tag{58a}$$

Where $\varphi_N(t)$ is the DTM's truncated series solution.

Considering that the term can be expressed in even power terms as follows:

$$\varphi_N(t) = \sum_{k=1}^{N} q_{1k} t^{1k} \tag{58b}$$

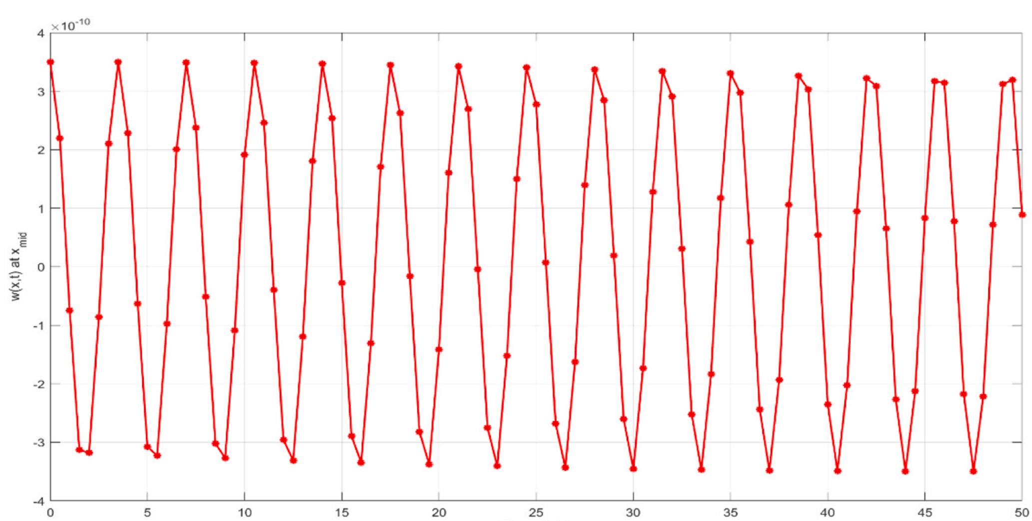

Fig 4.6. 3-D SWCNT's dynamic response at Mode 3.

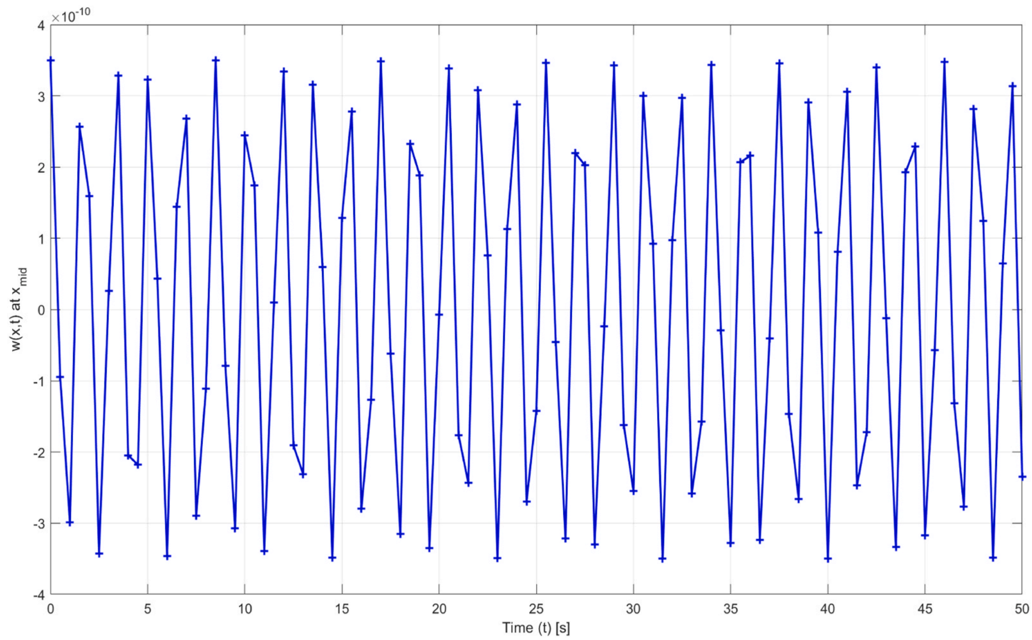

Fig. 4.7. SWCNT's midpoint dynamic response at mode 1.

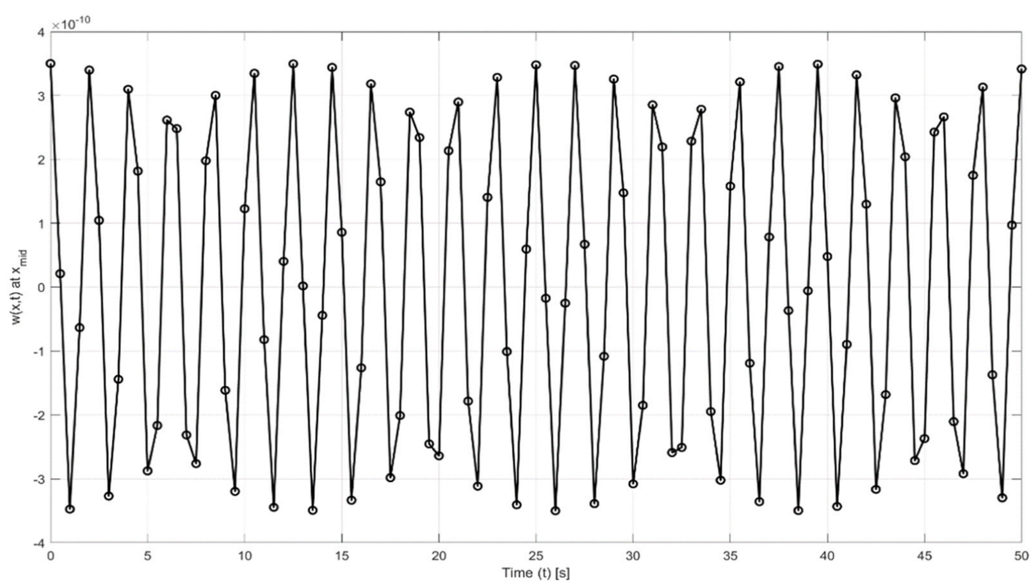

Fig. 4.8. SWCNT's midpoint dynamic response at mode 2.

This is put through:

$$\forall k = 0, 1, 2, \cdots, \frac{N}{2} - 1 \tag{58c}$$

The equivalent Sine equation is then given as:

$$\varphi_N(t) = \sum_{k=1}^{n} \mu_k \sin(\psi_k t) \tag{58d}$$

Then, using the Fourier series expansion, it becomes:

$$\varphi_N(t) = \left(\sum_{k=1}^{n} \mu_k {\psi_k}^1\right)\frac{t^1}{1} - \left(\sum_{k=1}^{n} \mu_k {\psi_k}^3\right)\frac{t^3}{3!} + \left(\sum_{k=1}^{n} \mu_k {\psi_k}^5\right)\frac{t^5}{5!} - \left(\sum_{k=1}^{n} \mu_k {\psi_k}^7\right)\frac{t^7}{7!} + \left(\sum_{k=1}^{n} \mu_k {\psi_k}^9\right)\frac{t^9}{9!}\cdots \tag{59}$$

The series solution of Eq. (58b) is given as:

$$\varphi_N(t) = q_1 t^1 + q_3 t^3 + q_5 t^5 + q_7 t^7 + \cdots + q_N t^N \tag{60}$$

By comparing both series solutions, we have:

$$q_1 t^1 + q_3 t^3 + q_5 t^5 + q_7 t^7 + \cdots + q_N t^N = \left(\sum_{k=1}^{n} \mu_k {\psi_k}^1\right)\frac{t^1}{1} - \left(\sum_{k=1}^{n} \mu_k {\psi_k}^3\right)\frac{t^3}{3!} + \left(\sum_{k=1}^{n} \mu_k {\psi_k}^5\right)\frac{t^5}{5!} - \cdots \tag{61}$$

By comparing coefficients, we have:

$$t^1 : \sum_{k=1}^{n} \mu_k \psi_k^1 = q_1$$

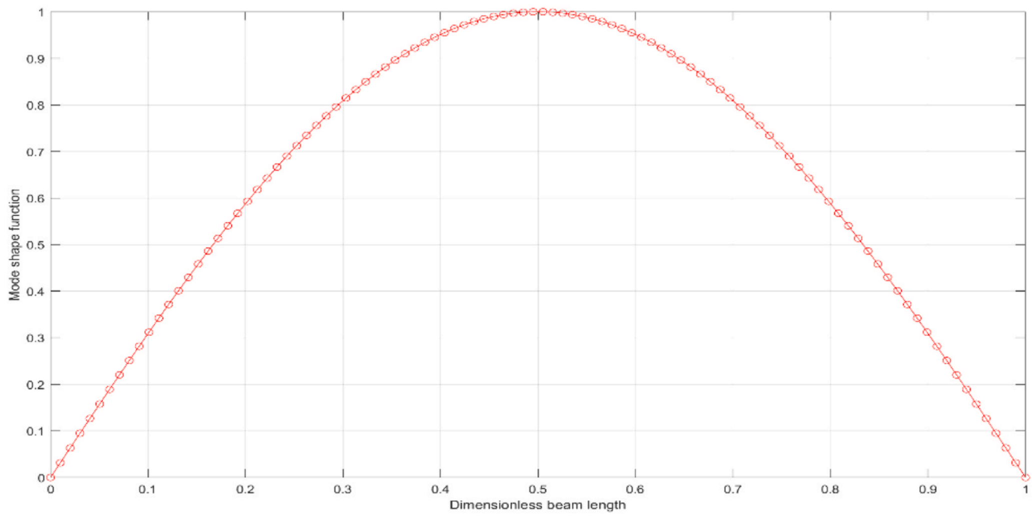

Fig. 4.9. SWCNT's midpoint dynamic response at mode 3.

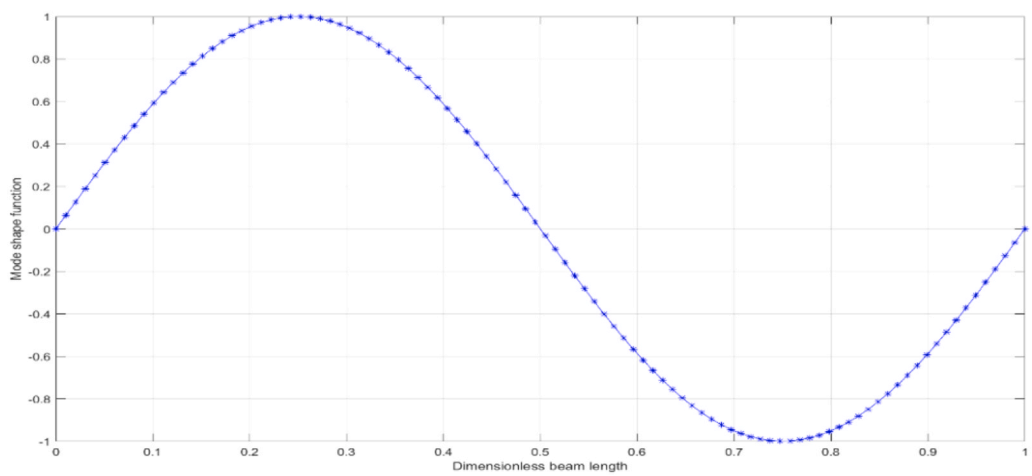

Fig. 4.10. Modal number's effect on the SWCNT's mode shape at mode 1.

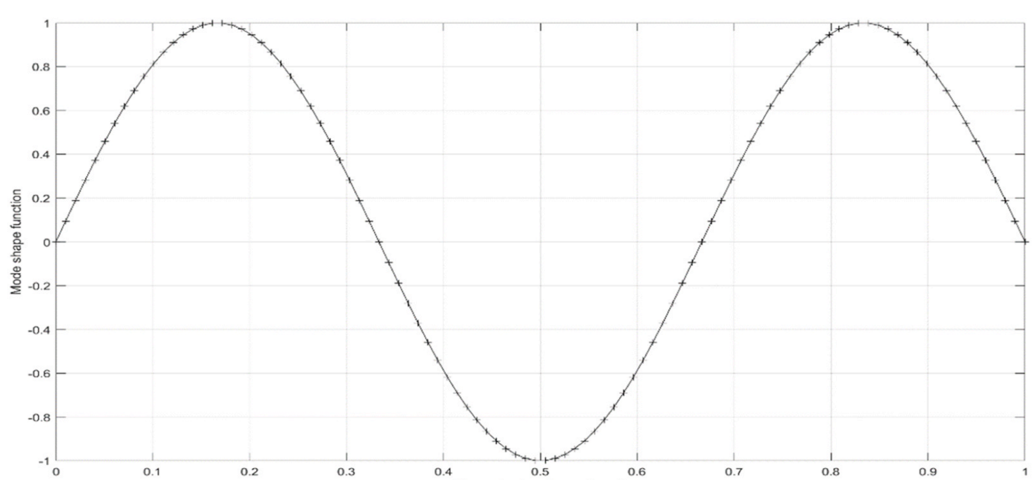

Fig. 4.11. Modal number's effect on the SWCNT's mode shape at mode 2.

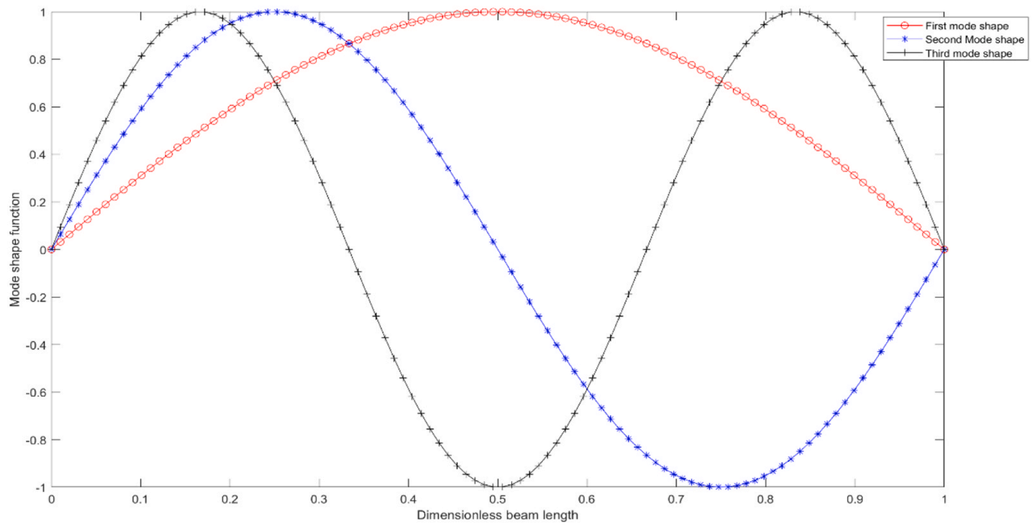

Fig. 4.12. Modal number's effect on the SWCNT's mode shape at mode 3.

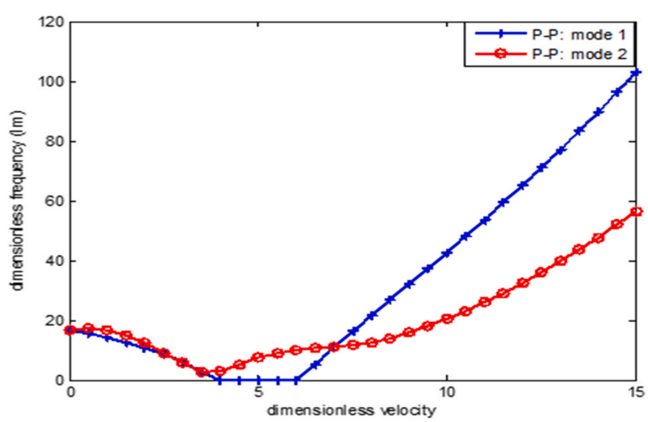

Fig. 4.13. This represents the superimposed plots of the three mode shapes.

$$t^3 : \sum_{k=1}^{n} \mu_k \psi_k^3 = -3! q_3$$

$$t^5 : \sum_{k=1}^{n} \mu_k \psi_k^5 = 5! q_5 \tag{62}$$

$$t^7 : \sum_{k=1}^{n} \mu_k \psi_k^7 = -7! q_7$$

An approximation of the expression in the form of a Sine function is given in place of these terms. This technique is described for the instance in which the truncation order (N) is 7. The goal is to express a function with two terms of Sine functions (n = 2). Which is:

$$\varphi_N(t) = \sum_{k=1}^{2} \mu_k \sin(\psi_k t) = \mu_1 \sin(\psi_1 t) + \mu_2 \sin(\psi_2 t)$$

Applying the technique/approach to Eq. (62) gives:

$$\begin{aligned} t^1 &: \mu_1\psi_1^1 + \mu_2\psi_2^1 = q_1 \\ t^3 &: \mu_1\psi_1^3 + \mu_2\psi_2^3 = -3! q_3 \\ t^5 &: \mu_1\psi_1^5 + \mu_2\psi_2^5 = 5! q_5 \\ t^7 &: \mu_1\psi_1^7 + \mu_2\psi_2^7 = -7! q_7 \end{aligned} \tag{63}$$

The four unknowns $\mu_1, \mu_2, \psi_1, \psi_2$ were found by obtaining solutions to the above system of non-linear algebraic equations using numerical methods.

From Eq. (32 - 37), the values of q were calculated and substituted into the SAT Eq. (63) is given as:

Mode n = 1

$$\begin{aligned} &\mu_1\psi_1^1 + \mu_2\psi_2^1 = 0 \\ &\mu_1\psi_1^3 + \mu_2\psi_2^3 = 0.00015273 \\ &\mu_1\psi_1^5 + \mu_2\psi_2^5 = -2.3034 \times 10^{26} \\ &\mu_1\psi_1^7 + \mu_2\psi_2^7 = -1.2407 \times 10^{56} \end{aligned}$$

Mode n = 2

$$\begin{aligned} &\mu_1\psi_1^1 + \mu_2\psi_2^1 = 0 \\ &\mu_1\psi_1^3 + \mu_2\psi_2^3 = 18.046 \\ &\mu_1\psi_1^5 + \mu_2\psi_2^5 = -4.7441 \times 10^{33} \\ &\mu_1\psi_1^7 + \mu_2\psi_2^7 = -4.4543 \times 10^{65} \end{aligned}$$

Mode n = 3

$$\begin{aligned} &\mu_1\psi_1^1 + \mu_2\psi_2^1 = 0 \\ &\mu_1\psi_1^3 + \mu_2\psi_2^3 = 0.013503 \\ &\mu_1\psi_1^5 + \mu_2\psi_2^5 = -6.8228 \times 10^{28} \\ &\mu_1\psi_1^7 + \mu_2\psi_2^7 = -1.2312 \times 10^{59} \end{aligned} \tag{64}$$

Eq. (64) are further solved simultaneously to yield the results in 4.1 to Table 4.6

3.3.3. *Combining CAT and SAT after treatment techniques*

For this case, the periodic solution is approximated as:

$$\varphi(t) = \lambda_1 \cos(\theta_1 t) + \lambda_2 \cos(\theta_2 t) + \mu_1 \sin(\psi_1 t) + \mu_2 \sin(\psi_2 t) \tag{65}$$

This is then solved by applying the solutions obtained from the CAT and SAT techniques using MATLAB software.

Therefore, we then obtain the displacement $w(x,t)$ by combining the special term obtained from the boundary condition and the temporal term obtained from after after-treatment.

$$w(x,t) = \Phi(x) \cdot \varphi(t) \tag{66}$$

This is rewritten as follows and is solved with the MATLAB software to obtain the displacement over a given period of time.

$$w\left(x,t\right) = \sin\left(\frac{n\pi}{L}x\right) \cdot \lambda_1 \cos(\theta_1 t) + \lambda_2 \cos(\theta_2 t) + \mu_1 \sin(\psi_1 t) + \mu_2 \sin(\psi_2 t) \tag{67}$$

Where $w(x,t)$ is the displacement

3.4. Machine learning model with XGBOOST

To predict SWCNT vibration characteristics based on input parameters, we train an XGBoost model using preprocessed data. To improve performance, model hyperparameters are tuned using strategies like random or grid search. Metrics like mean squared error (MSE) or mean absolute error (MAE) are then used to assess the model's performance on a validation dataset.

```
[ ]  target = [
         'mode1_theta1', 'mode1_theta2', 'mode1_lambda1', 'mode1_lambda2',
         'mode1_psi1', 'mode1_psi2', 'mode1_mu1', 'mode1_mu2', 'mode1_frequency',
         'mode2_theta1', 'mode2_theta2', 'mode2_lambda1', 'mode2_lambda2',
         'mode2_psi1', 'mode2_psi2', 'mode2_mu1', 'mode2_mu2', 'mode2_frequency',
         'mode3_theta1', 'mode3_theta2', 'mode3_lambda1', 'mode3_lambda2',
         'mode3_psi1', 'mode3_psi2', 'mode3_mu1', 'mode3_mu2', 'mode3_frequency'
     ]

     X=df.drop(target,axis=1)
     y=df[target]
```

```
[ ]  X_train, X_test, y_train, y_test = train_test_split(
         X,
         y,
         test_size=0.2,
         random_state=12
         )
```

```
xgb_model = MultiOutputRegressor(xgb.XGBRegressor(objective='reg:squarederror', random_state=42))
xgb_model.fit(X_train, y_train)
y_freq_pred_xgb = xgb_model.predict(X_test)
xgb_model.fit(X_train, y_train)
y_pred_xgb = xgb_model.predict(X_test)
```

```
feature_importances = []

for estimator in xgb_model.estimators_:
    importance = estimator.feature_importances_
    feature_importances.append(importance)
xgb_feature_importances = np.array(feature_importances)
xgb_mean_feature_importance = np.mean(feature_importances, axis=0)
for i, val in enumerate(xgb_mean_feature_importance):
    print(f"Feature {i+1}: {val}")
```

Show hidden output

```
[ ]  feature_names = X_train.columns

     plt.figure(figsize=(10, 6))
     plt.barh(feature_names, xgb_mean_feature_importance, color='brown')
     plt.xlabel('Mean Feature Importance')
     plt.ylabel('Features')
     plt.title('XGB Average Feature Importance Across All Targets')
     plt.show()
```

Code 1–2. : Machine learning model code 1 and 2

This shows the statistical exploration of the modes.

3.4.1. Backend development with python flask

The backend service acts as a bridge between the mobile application and the machine learning model/database. It takes queries from the mobile app, processes them by sending the machine learning model parameters to make predictions or by requesting information from the database, stores pertinent data in the database, and then sends the appropriate response back to the mobile app.

3.4.2. Mobile development with flutter

The Flutter-developed mobile application has a user-friendly interface that prompts users to interact with buttons that invoke the backend API in order to enter necessary parameters and generate data. The data is generated, and the user is presented with the results, including graphs for visual aids.

4. Results and discussion

To obtain the solution for the displacement of the SWCNT over a period from simulations and to ascertain how different model parameters affect the SWCNT's dynamic response, which is displayed via graphs and tables. The parameters used in obtaining these data were varied and, on a Nano-scale to train the machine learning models with varying data

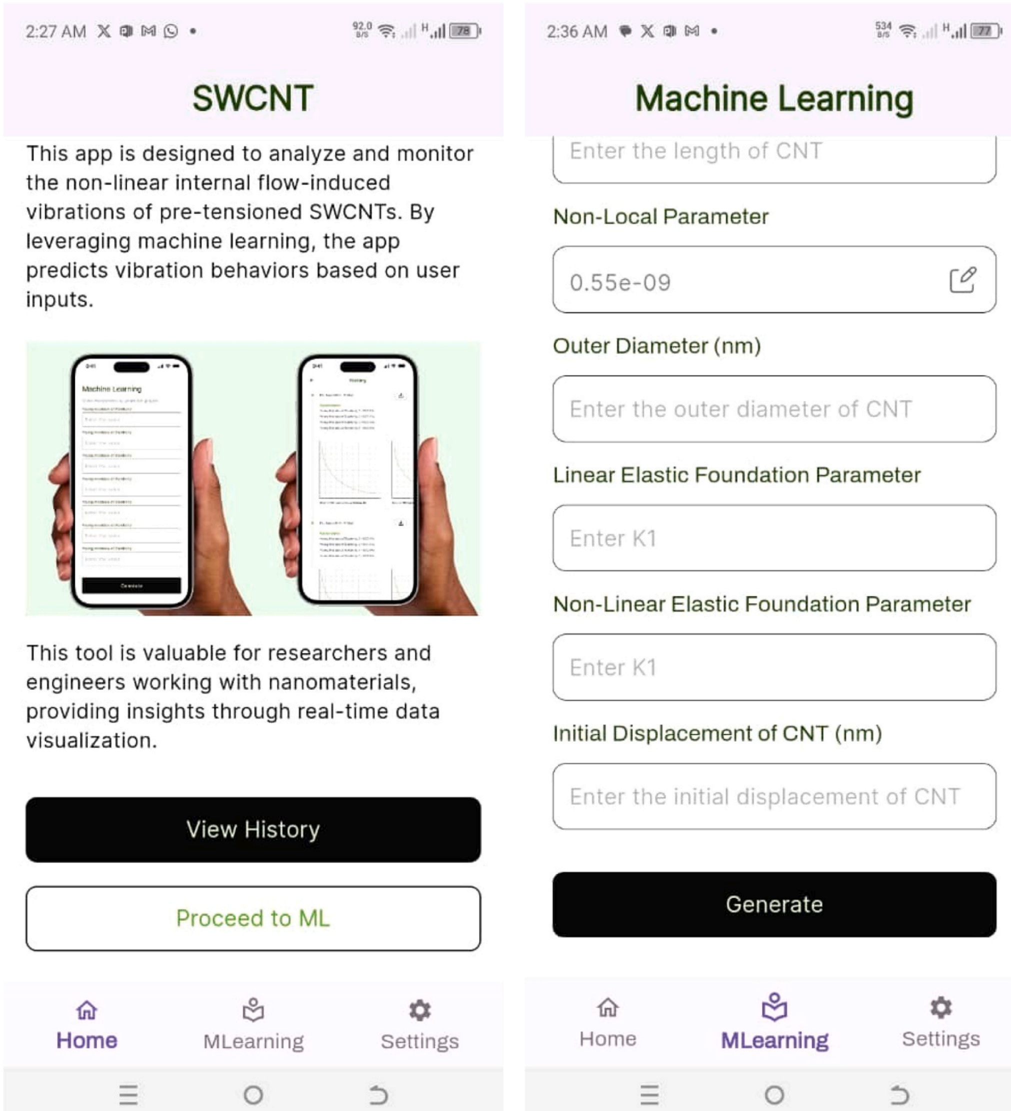

Fig. 4.14. Plot of Natural frequency against frequency for pinned-pinned SWCNT.

and for optimal accuracy.

4.1. Table of values after the after-treatment techniques

See Table 4.1-4.6

4.2. Dynamic response analysis of SWCNTs

Fig. 4.1 shows the dynamic response of SWCNT after the CAT and SAT techniques. The periodic nature of the deflection indicates resonance or excitation of specific vibrational modes. These vibrations are caused by various forces influencing the nanotube. At Mode 1, the response is relatively stable with a smoother amplitude, suggesting that the nanotube can maintain steady vibration with minimal instability.

Fig. 4.2 depicts the dynamic response of SWCNT at mode 2 after the after-treatment techniques are applied to generate a dynamic response over a period.

Fig. 4.3 depicts the dynamic/periodic response of SWCNT at mode 3 after the CAT and SAT technique is applied, and the temporal response is obtained over a period. The corresponding three-dimensional plots are depicted in Figs 4.4 – 4.6.

By contrast, Modes 2 and 3 reveal sharper fluctuations and stronger nonlinearities, indicating a reduced ability to maintain equilibrium. This progression illustrates that higher vibrational modes amplify sensitivity to flow velocity and external disturbances, a critical factor in applications requiring long-term structural reliability.

Figs 4.4 – 4.6 depict the 3-dimensional dynamic response of the deflection at different spatial and temporal conditions at different modes. This is obtained after the after-treatment techniques have been done on the analytically solved model under a simply supported boundary condition. The visualization in three dimensions, therefore, not only confirms the periodicity achieved through after-treatment techniques but also offers a practical way of interpreting vibrational behavior in real applications, such as Nano-electromechanical devices and sensing technologies.

From the plots, it is evident that even modes give a stable amplitude of vibration for temporal deflection plots. These plots help denote regions of nodes and anti-nodes for structural enhancement and brazing, where and when necessary.

4.3. Three-dimensional dynamic response of SWCNT

See Fig. 4.4

4.4. Midpoint deflection $w(x, t)$ OF SWCNT at different modes

Figs. 4.7 – 4.9 denote the dynamic responses at the midpoint deflection of the SWCNT. This deflection of the SWCNT was obtained through the treated model using CAT and SAT techniques for a Pinned-Pinned boundary condition SWCNT. To achieve these simulations, the modal number in the solution's spatial term is varied as the generalized deflection result is plotted against time. This gives the SWCNT's dynamic response. Subsequently, the deflection history of the nanostructure can be obtained, remodeled, and used to generate a predictive model. The midpoint response is particularly important because it represents the location of maximum bending stress in a pinned–pinned nanotube. The observed rise in oscillation frequency and amplitude with mode number shows that greater vibrational states make the nanotube more prone to fatigue and long-term instability near its midpoint.

4.5. Effect of modal number on the SWCNT'S mode shape

The vibration of the pinned-pinned SWCNT for modes 1, 2, and 3 is shown along the dimensionless beam length in Figs. 4.10 - 4.13. The plot makes it clear that an increase in mode number decreases SWCNT stability since it causes the system's frequency and number of cycles to grow proportionately for an equivalent beam length. Higher mode shapes indicate that the nanotube experiences more rapid oscillations along its length. This leads to a redistribution of strain energy across the structure, which affects overall stability. These happen because of the trial function's dependence on modal numbers.

4.6. Stability responses of the swcnt under different modes

Fig. 4.14 shows the stability responses of the nanotube under different modes. It is evident from the plots that an increase in the mode number decreases the stability of the nanotube. For higher modes, the nanotube also finds it difficult to regain stability after bifurcation. This makes the nanotube approach instability and prone to flutter as the velocity of flow is increased above the critical point. When flutter occurs, the nanotube is unable to disperse the energy input from the flow, as the stability study shows. The significance of operating devices based

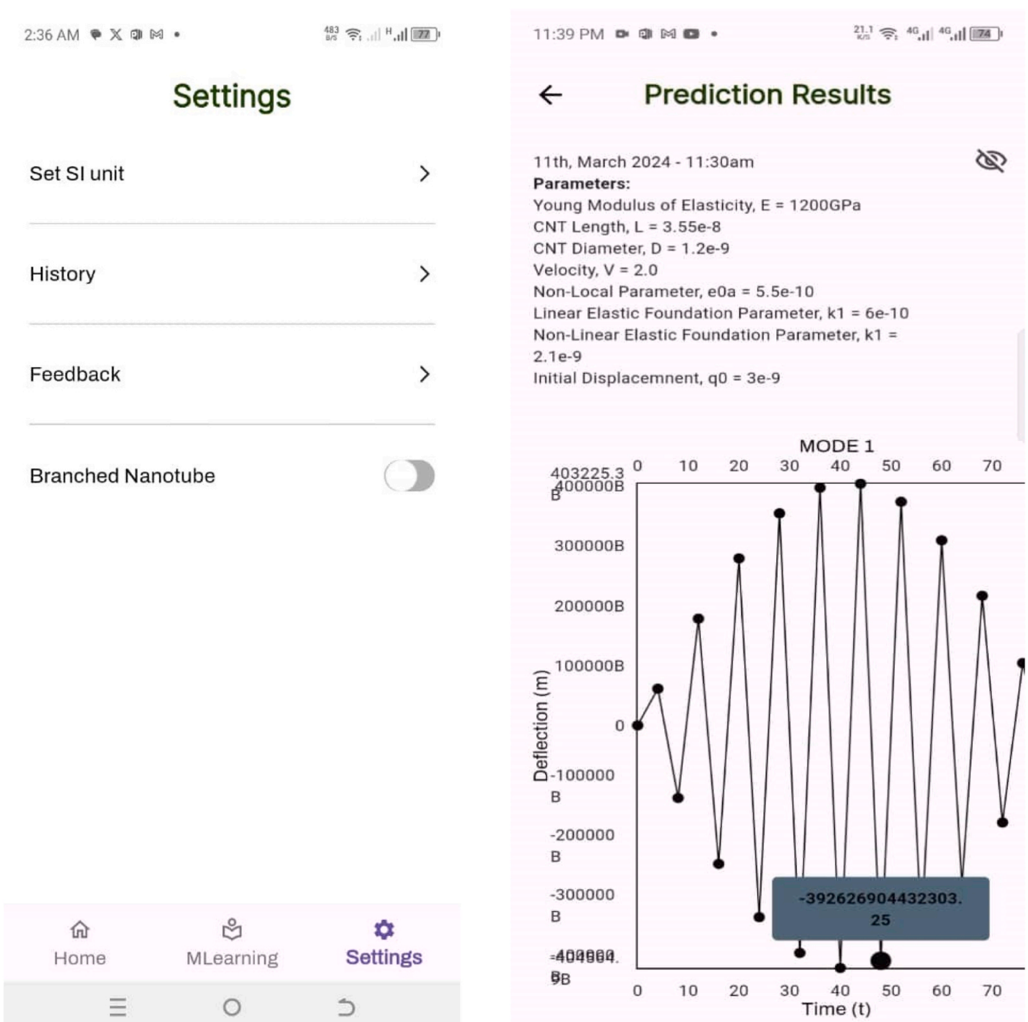

Fig. 4.15. (a-b): Mobile application Home page and Machine learning screens (c-d): Mobile application Settings and Prediction results screens. The input parameters were supplied to the Machine learning input page to generate the graphs of the deflection of the SWCNT against Time (e-f): Mobile Application's Plot screens. The application generates both two-dimensional and three-dimensional plots for the parameters supplied by the user.

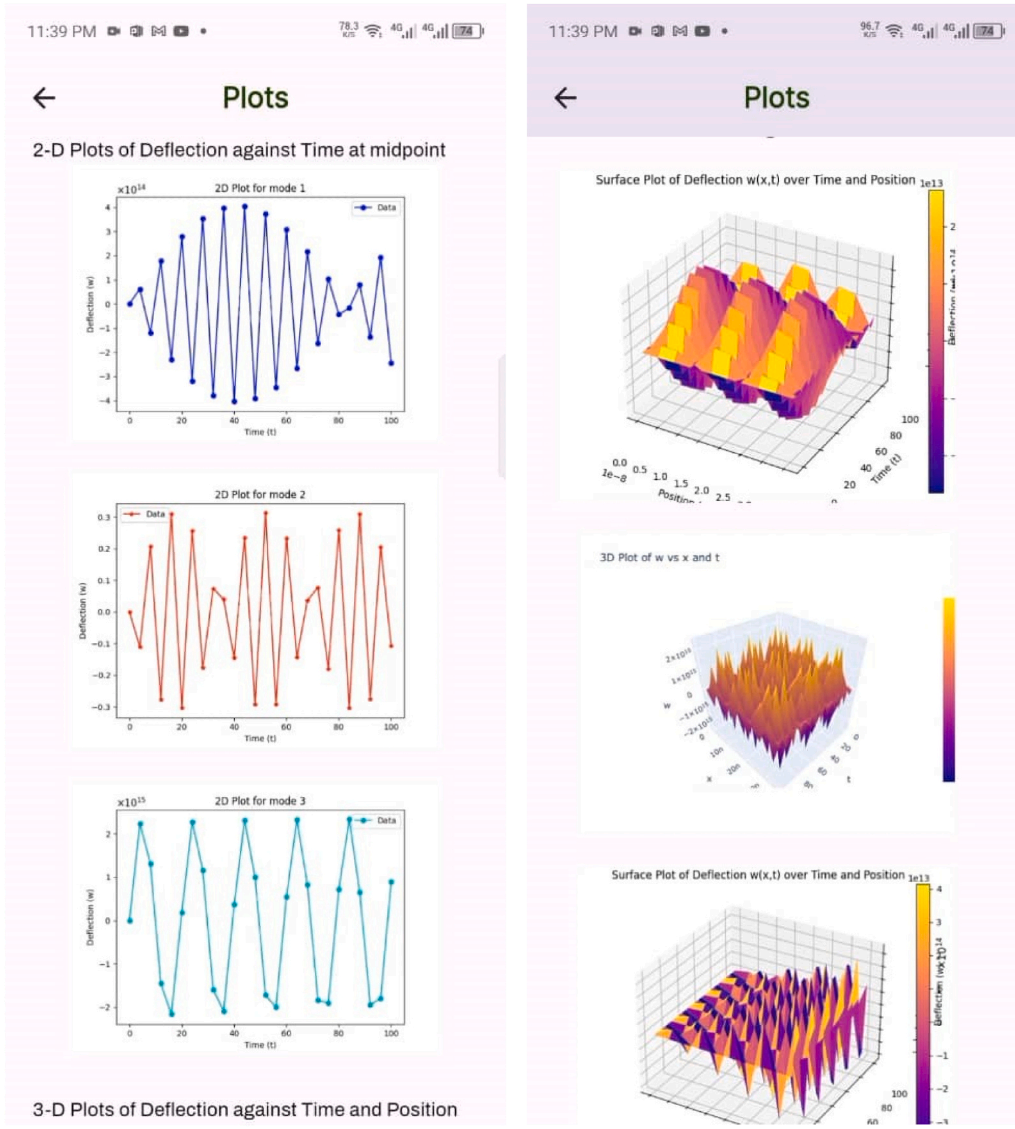

Fig. 4.15. (*continued*).

on nanotubes below their critical flow velocity is shown by this outcome.

4.7. Visualization of the mobile app development with flutter

Leveraging the user-friendly nature of the mobile application developed with Flutter, the necessary parameters for the vibration of the nanotube are supplied as requested, and the necessary data are generated. These data are visualized and used for predictive analysis, as shown in Fig 4.15

5. Conclusion

This paper investigated the dynamic response and vibration characteristics of SWCNTs under varying conditions. This study employed a combination of theoretical modeling, data analysis, Machine learning, and Software development to explore the effects of various variables on the nanotube's behavior. The equation of motion of the nanotube was derived and solved using the DTM. CAT and SAT after-treatment techniques were applied to ensure the solution's validity over extended time domains. The data obtained from the analytical solution over a varying parameter were used to train the machine learning model, which accepts parameters from users and returns the predicted data as expected. These data are displayed as graphs and charts on the mobile application for effective visualization and to monitor the effect of these varying parameters on the dynamic response of the Single-Walled Carbon Nanotube. From the work, it was concluded that:

- A rise in modal number reduces the stability of the nanotube.
- For higher modes, the nanotube finds it difficult to regain stability after bifurcation.
- Nanotube approaches flutter as the velocity of flow is increased beyond the critical point.
- Machine Learning can be used to train data from vibration analysis for visualization and predictive purposes.
- The employed solution techniques work for the problems investigated.

Overall, this paper offers two main advantages: the combination of Galerkin decomposition, DTM, and after-treatment techniques provides robust analytical solutions for nonlinear vibration problems, and the integration with machine learning and mobile visualization tools improves accessibility, interpretation, and practical application of the results. These contributions not only advance the understanding of SWCNT vibrational behavior but also provide a scalable framework for future studies in nanomaterials and smart engineering systems.

Declaration of Competing Interest

The authors declare that they have no known competing financial interests or personal relationships that could have appeared to influence the work reported in this paper.

References

[1] F. Lu, Z. He, N. She, A. Yabushita, D. Uchida, Y. Maeda, T. Kobayashi, Ultrafast electronic dynamics and vibrational dynamics of SWCNT under alkylation and annealing, Chem. Phys. 553 (2022) 111387, https://doi.org/10.1016/j.chemphys.2021.111387.

[2] A.A. Yinusa, M.G. Sobamowo, Nonlinear thermal-magneto-mechanical vibration analysis of single-walled embedded branched carbon nanotubes conveying nanofluid, ASME J. Eng. 2 (2023) 021035, https://doi.org/10.1115/1.4062695.

[3] A.A. Yinusa, M.G. Sobamowo, Mechanics of nonlinear internal flow induced vibration and stability analysis of a pre-tensioned single-walled carbon nanotube using classical differential transform method with CAT and SAT after treatment techniques, Forces Mech. 7 (2022) 100083, https://doi.org/10.1016/j.finmec.2022.100083.

[4] A. Ali, E.N. Tugolukov, Review enhancement of thermal conductivity and heat transfer using carbon nanotube for nanofluids and ionanofluids, J. Therm. Eng. 7 (2021) 66–90, https://doi.org/10.18186/thermal.843077.

[5] A. Mohamed, M. Eltaher, M. Nazira, Nonlinear stability and vibration of imperfect CNTs by doublet mechanics, Appl. Math. Comput. 383 (2020) 123–311, https://doi.org/10.1016/j.amc.2020.125311.

[6] N. Herisanu, B. Marinca, V. Marinca, Nonlinear vibration of double-walled carbon nanotubes subjected to mechanical impact and embedded on Winkler–Pasternak foundation, Materials 15 (23) (2021) 8599, https://doi.org/10.3390/ma15238599.

[7] D. Miyashiro, H. Taira, R. Hamano, R.L. Reserva, K. Umemura, Mechanical vibration of single-walled carbon nanotubes at different lengths and carbon nanobelts by modal analysis method, Compos. Part C Open Access 2 (2020) 100028, https://doi.org/10.1016/j.jcomc.2020.100028.

[8] S. Oveissi, M. Salehi, A. Ghassemi, S. Ali Eftekhari, S. Ziaei-Rad, Energy harvesting of nanofluid-conveying axially moving cylindrical composite nanoshells of integrated CNT and piezoelectric layers with magnetorheological elastomer core under external fluid vortex-induced vibration, J. Magn. Magn. Mater. 572 (2023) 170551, https://doi.org/10.1016/j.jmmm.2023.170551.

[9] Ahmed, W., Elhissi, A., Dhanak, V. and Subramani, K. (2017) Carbon nanotubes: Applications in cancer therapy and drug delivery research. In: Emerging Nanotechnologies in Dentistry (Second Edition), pp. 371-389. https://doi.org/10.1016/B978-0-12-812291-4.00018-2.

[10] M. Canadija, Deep learning framework for carbon nanotubes: mechanical properties and modeling strategies, Carbon 184 (2021) 891–901, https://doi.org/10.1016/j.carbon.2021.08.091.

[11] L.E. Vivanco-Benavides, C.L. Martínez-González, C. Mercado-Zúñiga, C. Torres-Torres, Machine learning and materials informatics approaches in the analysis of physical properties of carbon nanotubes: a review, Comput. Mater. Sci. 201 (2021) 110939, https://doi.org/10.1016/j.commatsci.2021.110939.

[12] G.D. Forster, A. Castan, A. Loiseau, J. Nelayah, D. Alloyeau, F. Fossard, C. Bichara, H. Amara, A deep learning approach for determining the chiral indices of carbon nanotubes from high-resolution transmission electron microscopy images, Carbon 169 (2020) 465–474, https://doi.org/10.1016/j.carbon.2020.06.086.

[13] M. Dewapriya, R. Rajapakse, W. Dias, Characterizing fracture stress of defective graphene samples using shallow and deep artificial neural networks, Carbon 163 (2020) 425–440, https://doi.org/10.1016/j.carbon.2020.03.038.

[14] H.P. Lal, A. B.R, D. Ghosh, Prediction of nonlocal elasticity parameters using high-throughput molecular dynamics simulations and machine learning, Eur. J. Mech. A/Solids 103 (2023) 105175, https://doi.org/10.1016/j.euromechsol.2023.105175.

[15] A. Beitollahi, M. Janghorban, Y. Bazargan-Lari, A. Tounsi, On the variable length scale parameter for agglomeration of nanoparticles in nanocomposites, Proceedings Institution Mechanical Engineers Part C Journal Mechanical Engineering Science 239 (10) (2025) 3828–3850, https://doi.org/10.1177/09544062241308513.

[16] Bousmaha, K., Belalia, S.A., Chorfi, S.M., Tounsi, A., Al-Osta, M.A., & Alluqmani, A.E. (Accepted/In press). On the dynamic behavior of plates made of porous advanced materials reinforced with carbon nanotubes using a p-version of finite element method. Mechanics Based Design of Structures and Machines. https://doi.org/10.1080/15397734.2025.2534679.

[17] Q. Gawah, M.A. Abdullah, M.A. Al-Osta, F. Bourada, A. Tounsi, M. Yaylacı, Free vibration analysis of nonlinearly dispersed FG-CNTRC beams on kerr substrate using an improved FSDT, Struct. Eng. Mech. 93 (6) (2025) 475–493, https://doi.org/10.12989/sem.2025.93.6.475.

[18] H. Youzera, S.A. Meftah, A. Tounsi, M.A. Salem, K.M. Khedher, M. Yaylacı, Nonlinear forced vibration analysis of FG-CNTRC sandwich beams with viscoelastic core under various boundary conditions, Mech. Adv. Mater. Struct. (2025) 1–10, https://doi.org/10.1080/15376494.2025.2473691.

[19] H. Youzera, S.A. Meftah, A. Tounsi, et al., Free vibration analysis of sandwich cylindrical shells with functionally graded carbon nanotube-reinforced composite face sheets using the differential quadrature (DQ) method, Acta Mech. 236 (2025) 1395–1410, https://doi.org/10.1007/s00707-025-04230-y.

[20] S. Al-Houri, M.A. Al-Osta, Q. Gawah, F. Bourada, A. Tounsi, S.U. Al-Dulaijan, A. Tounsi, Wave propagation analysis of composite beams reinforced with nonlinear FG-CNT distributions supported on kerr elastic foundation utilizing an improved integral first-order shear deformation theory, Geomech. Eng. 39 (5) (2024) 483–501, https://doi.org/10.12989/GAE.2024.39.5.483.

[21] A. Tounsi, Z. Belabed, F. Bounouara, M. Balubaid, S.R. Mahmoud, A.A. Bousahla, A. Tounsi, A finite element approach for forced dynamical responses of porous FG nanocomposite beams resting on viscoelastic foundations, Int. J. Struct. Stab. Dyn. 24 (6) (2024) 2450078, https://doi.org/10.1142/S0219455426500781.

[22] R. Zerrouki, M. Zidour, A. Tounsi, A. Tounsi, Z. Belabed, A.A. Bousahla, M. A. Salem, K.M. Khedher, Buckling behavior of nonlinear FG-CNT reinforced nanocomposite beam reposed on Winkler/Pasternak foundation, Comput. Concr. 34 (3) (2024) 297–305, https://doi.org/10.12989/cac.2024.34.3.297.

[23] A.M. Alsubaie, M.A. Al-Osta, I. Alfaqih, A. Tounsi, A. Chikh, I.M. Mudhaffar, S. U. Al-Dulaijan, S. Tahir, Influences of porosity distributions on bending and buckling behaviour of functionally graded carbon nanotube-reinforced composite beam, Comput. Concr. 34 (2) (2024) 179–193, https://doi.org/10.12989/cac.2024.34.2.179.

[24] S. Boutaleb, A. Boulal, M. Zidour, M.A. Al-Osta, A. Tounsi, A. Tounsi, M.A. Salem, K.M. Khedher, On the buckling response of functionally graded carbon nanotube-reinforced composite imperfect beams, Period. Polytech. Civ. Eng. 68 (4) (2024) 1052–1063, https://doi.org/10.3311/PPci.23825.

[25] A.M. Alsubaie, I. Alfaqih, M.A. Al-Osta, A. Tounsi, A. Chikh, I.M. Mudhaffar, S. Tahir, Porosity-dependent vibration investigation of functionally graded carbon nanotube-reinforced composite beam, Comput. Concr. 32 (1) (2023) 75–85, https://doi.org/10.12989/cac.2023.32.1.075.

[26] E. Madenci, Y.O. Özkiliç, A. Hakamy, A. Tounsi, Experimental tensile test and micro-mechanic investigation on carbon nanotube reinforced carbon fiber composite beams, Adv. Nano Res. 14 (5) (2023) 443–450, https://doi.org/10.12989/anr.2023.14.5.443.

[27] Z. Belabed, A.A. Bousahla, A. Tounsi, Vibrational and elastic stability responses of functionally graded carbon nanotube reinforced nanocomposite beams via a new Quasi-3D finite element model, Comput. Concr. 34 (5) (2024) 625–648, https://doi.org/10.12989/cac.2024.34.5.625.

[28] M. Hussain, M.A. Khadimallah, A. Tounsi, Correlation between frequency and Poisson's ratio: study of durability of armchair SWCNTs, Comput. Concr. 32 (3) (2023) 303–311, https://doi.org/10.12989/cac.2023.32.3.303.

[29] M. Hussain. Small-scale Computational Vibration of Carbon Nanotubes: Composite Structure, (1st ed.)., River Publishers, 2024 https://doi.org/10.1201/9781032656229.

[30] E. Ghandourah, M. Hussain, F.A. Thobiani, M. Hefni, S. Alghamdi, Direct strength measurement of Timoshenko-beam model: vibration analysis of double walled carbon nanotubes, Struct. Eng. Mech. 84 (1) (2022) 77–83, https://doi.org/10.12989/SEM.2022.84.1.077.

[31] M.A. Khadimallah, I. Harbaoui, J.B. Casimir, L.H. Taieb, M. Hussain, A. Tounsi, Continuous element method for aeroacoustic' waves in confined ducts, Adv. Nano Res. 13 (4) (2022) 341–351, https://doi.org/10.12989/anr.2022.13.4.341.

[32] S. Asghar, M. Hussain, M.A. Khadimallah, M.N. Naeem, Z. Ali, K.M. Khedher, M. Taj, A. Tounsi, Prediction of small-scale vibration of zigzag DWCNTs: numerical approach, Steel Compos. Struct. 39 (6) (2021) 781–793, https://doi.org/10.12989/scs.2021.39.6.781.

[33] M. Hussain, Application of Kelvin's approach for material structure of CNT: polynomial volume fraction law, Struct. Eng. Mech. 76 (1) (2020) 129–139, https://doi.org/10.12989/sem.2020.76.1.129.

[34] M. Hussain, A. Selmi, Analytical vibration of FG cylindrical shell with ring support based on various configurations, Adv. Concr. Constr. 9 (6) (2020) 557–568, https://doi.org/10.12989/ACC.2020.9.6.557.

[35] E. Karbassiyazdi, F. Fattahi, N. Yousefi, A. Tahmassebi, A.A. Taromi, J.Z. Manzari, A.H. Gandomi, A. Altaee, A. Razmjou, XGBoost model as an efficient machine learning approach for PFAS removal: effects of material characteristics and operation conditions, Environ. Res. 215 (2022) 114286, https://doi.org/10.1016/j.envres.2022.114286.

[36] Y. Hua, S. Xie, X. Jin, A novel sampled-data asynchronous CatBoost model with knowledge-based guidance for product quality estimation in the industrial processes, Measurement 225 (2024) 114024, https://doi.org/10.1016/j.measurement.2023.114024.

[37] A. Sudheer Kumar, S. Dayam, K. Desai, Wear monitoring solution for end mills using deep learning and mobile application, Manuf. Lett. 35 (2023) 1127–1133, https://doi.org/10.1016/j.mfglet.2023.08.111.